

1 **Combining CRISPR/Cas9 and brain imaging: from genes to molecules**
2 **to networks**

3 Sabina Marciano¹, Tudor Mihai Ionescu¹, Ran Sing Saw¹, Rachel Y. Cheong², Deniz Kirik²,
4 Andreas Maurer¹, Bernd Pichler¹, Kristina Herfert^{1*}

5

6

7

8

9

10

11 ¹Werner Siemens Imaging Center, Department of Preclinical Imaging and Radiopharmacy,
12 Eberhard Karls University Tuebingen, Germany

13 ²Brain Repair and Imaging in Neural Systems, Department of Experimental Medical Science,
14 Lund University, Sweden

15

16 *Corresponding author: Prof. Dr. Kristina Herfert (kristina.harfert@med.uni-tuebingen.de)

17

18 Address: Roentgenweg 13, 72076 Tuebingen, Germany, Tel: +49 7071 29 87680

19

20 **Abstract**

21 Receptors, transporters and ion channels are important targets for therapy development in
22 neurological diseases including Alzheimer's disease, Parkinson's disease, epilepsy,
23 schizophrenia and major depression. Several receptors and ion channels identified by next
24 generation sequencing may be involved in disease initiation and progression but their
25 mechanistic role in pathogenesis is often poorly understood. Gene editing and *in vivo* imaging
26 approaches will help to identify the molecular and functional role of these targets and the
27 consequence of their regional dysfunction on whole brain level. Here, we combine CRISPR/Cas9
28 gene-editing with *in vivo* positron emission tomography (PET) and functional magnetic resonance
29 imaging (fMRI) to investigate the direct link between genes, molecules, and the brain
30 connectome. The extensive knowledge of the *Slc18a2* gene encoding the vesicular monoamine
31 transporter (VMAT2), involved in the storage and release of dopamine, makes it an excellent
32 target for studying the gene networks relationships while structurally preserving neuronal integrity
33 and function. We edited the *Slc18a2* in the substantia nigra pars compacta of adult rats and used
34 *in vivo* molecular imaging besides behavioral, histological, and biochemical assessments to
35 characterize the CRISPR/Cas9-mediated VMAT2 knockdown. Simultaneous PET/fMRI was
36 performed to investigate molecular and functional brain alterations. We found that stage-specific
37 adaptations of brain functional connectivity follow the selective impairment of presynaptic
38 dopamine storage and release. Our study reveals that recruiting different brain networks is an
39 early response to the dopaminergic dysfunction preceding neuronal cell loss. Our combinatorial
40 approach is a novel tool to investigate the impact of specific genes on brain molecular and
41 functional dynamics which will help to develop tailored therapies for normalizing brain function.
42 The method can easily be transferred to higher-order species allowing for a direct comparison of
43 the molecular imaging findings.

44

45

46

47 **Keywords**

48 CRISPR/Cas9, Functional Connectivity, Dopamine, VMAT2, D2 receptor, [¹¹C]raclopride,

49 PET/fMRI.

50

51 **Introduction**

52 The brain is a network of spatially distributed but functionally and structurally interconnected
53 regions that exhibit correlated activity over time. They communicate with each other via highly
54 specialized neuronal connections and are organized in neuronal circuits and networks.
55 Understanding how functional connections between regions are arranged in the healthy and
56 diseased brain is therefore of great interest.

57 Resting-state functional magnetic resonance imaging (rs-fMRI) has enabled neuroscientists to
58 delineate the level of functional communication between anatomically separated regions [1]. Rs-
59 fMRI measures the resting-state functional connectivity (rs-FC) at high spatial and temporal
60 resolutions based on spontaneous fluctuations of the blood oxygen level-dependent (BOLD)
61 signal at rest, which indirectly detects neuronal activity via hemodynamic coupling [2]. Using rs-
62 fMRI several brain resting-state networks in humans and rodents have been identified, such as
63 the default mode and sensorimotor networks (DMN, SMN) [3-9]. Alterations of these networks are
64 linked to neurological diseases [10, 11], and may serve as early therapeutic and diagnostic
65 biomarkers. However, the molecular signatures related to the functional alterations in disease
66 remain largely unknown.

67 Positron emission tomography (PET) provides a non-invasive tool to indirectly measure molecular
68 changes in the brain with high specificity and sensitivity. One well-characterized example is the
69 radioligand [¹¹C]raclopride, a widely used D2/D3 receptor antagonist enabling the non-invasive
70 determination of dopamine release and availability [12-14].

71 PET in combination with BOLD-fMRI has the great potential to investigate the molecular
72 substrate of brain functional connectivity (FC), enabling the direct spatial and temporal correlation
73 of both measurements [15-21]. In this context, we have recently shown that rs-FC is modulated
74 by intrinsic serotonin transporter and D2/3 receptor occupancy in rats [22].

75 Insights into functional brain circuits and their relationships to individual phenotypes can be
76 gained by genetic manipulations of neuronal subtypes [23]. Genome-engineering methodologies
77 based on clustered regularly interspaced short palindromic repeats (CRISPR)/associated RNA-
78 guided endonuclease (Cas9) represent a promising approach to unveil the influence of genes on
79 brain circuits. CRISPR/Cas9 has enabled researchers to interrogate the mammalian DNA in a
80 precise yet simple manner [24, 25] in several species [26-31], by editing single or multiple
81 genomic loci *in vitro* and *in vivo* [25, 32, 33]. However, one great hurdle is the brain delivery,
82 which must comply with effective nuclear access, while minimizing immunogenic reactions and
83 off-target editing [34]. Despite these limitations, the potential of CRISPR/Cas9 is continuously
84 expanding with novel nuclease variants being exploited [35-37]. Derived from *Staphylococcus*
85 *aureus*, SaCas9 overcomes the packaging constraints of adeno-associated viral vectors (AAVs),
86 allowing efficient CRISPR/Cas9 brain transfer [38-42].

87 Here, we use an AAV-based CRISPR/SaCas9 gene-editing approach to knock down the *Slc18a2*
88 gene encoding the vesicular monoamine transporter 2 (VMAT2), a key protein involved in the
89 storage and release of dopamine in the brain [43]. The extensive knowledge on *Slc18a2* makes it
90 an excellent basis for studying the gene networks relationships. We characterize the VMAT2-
91 mediated dopamine signaling using *in vivo* molecular imaging, behavioral, histological, and
92 biochemical assessments. We investigate the impact of impaired VMAT2-dependent dopamine
93 neurotransmission on the DMN and SMN using a simultaneous $[^{11}\text{C}]$ raclopride-PET/fMRI
94 protocol. Further, we dig into the dopamine-GABA interplay using $[^{11}\text{C}]$ flumazenil PET. Our
95 results reveal that CRISPR/SaCas9-induced synaptic dysfunction prompts early network
96 changes, preceding motor and molecular alterations, including a regional increase in postsynaptic
97 dopamine receptor availability. We identify a pattern of asymmetric hyperconnectivity, and
98 internetwork synchronization, spreading from the contralateral thalamus (SMN), and prefrontal
99 cortical regions (DMN) to the striata and hippocampi, complemented by a reduced GABA-A
100 receptor availability.

101 Our findings illustrate the ability of the brain to recruit different brain networks and functionally
102 compensate for the dopaminergic dysfunction prior to neuronal cell loss, postsynaptic changes,
103 and motor impairment.

104

105 **Results**

106 ***In vitro validation of CRISPR/SaCas9-induced VMAT2 knockdown in rat primary cortical***
107 ***neurons***

108 To evaluate the efficiency of the AAV-based CRISPR/SaCas9 VMAT2 knockdown in rat primary
109 neurons, we designed AAV-SaCas9 and AAV-sgRNA targeting the first exon of the bacterial *lacZ*
110 gene (control) or the second exon of the *Slc18a2* gene (Fig. 1a) (sgRNAs sequences are
111 reported in Table 1). Seven days post-transduction, the protein expression level and mutation
112 rate of the harvested genomic DNA were inspected by immunofluorescence and surveyor assay
113 (Fig. 1b). Immunofluorescence indicated a clear reduction of VMAT2 protein expression in
114 neurons transduced with AAV-SaCas9 and AAV-sgRNA-*Slc18a2* (Fig. 1c). We observed 20%
115 editing for the digested DNA from neurons transduced with vectors for SaCas9 and sgRNA-
116 *Slc18a2* (Supplementary Fig.1).

117

118 ***CRISPR/SaCas9-induced VMAT2 knockdown elicits postsynaptic changes but no nerve***
119 ***terminal loss or neuroinflammation in the adult rat brain***

120 To test the *in vivo* efficiency of the CRISPR/SaCas9 gene-editing, we expressed SaCas9 and
121 sgRNA targeting *Slc18a2* to knock down the VMAT2, or targeting *lacZ* as control, by AAV-
122 mediated gene transfer into the right substantia nigra pars compacta (SNc). DPBS was injected
123 into the left SNc. [¹¹C]Dihydrotetrabenazine (DTBZ) PET imaging was performed 8 – 10 weeks
124 post-injection to quantify VMAT2 expression in the striatum (Fig. 2a).

125 $[^{11}\text{C}]$ DTBZ binding was decreased by 30% (0-62%) in the right striatum of rats where the VMAT2
126 was knocked down in comparison to the contralateral striatum. No changes of $[^{11}\text{C}]$ DTBZ binding
127 were observed in the contralateral striatum, as $[^{11}\text{C}]$ DTBZ binding did not differ between the left
128 striatum of rats injected with sgRNA targeting *lacZ* and rats injected with sgRNA targeting
129 *S/c18a2* (Fig. 2b,c).

130 We further evaluated changes of dopamine availability in the striatum using $[^{11}\text{C}]$ raclopride, which
131 competes with dopamine for the same binding site at the D2 receptor (D2R) [13]. After 12 –
132 14 weeks following CRISPR/SaCas9-induced VMAT2 knockdown in nigrostriatal neurons, we
133 observed 17% increased binding of $[^{11}\text{C}]$ raclopride in the right striatum of VMAT2 knockdown rats
134 and no changes in control rats (Fig. 2b,c), indicating a reduction of synaptic dopamine levels
135 and/or compensatory changes of D2R expression at postsynaptic medium spiny neurons. A
136 larger VMAT2 knockdown led to lower dopamine levels in the striatum and thus to higher D2R
137 binding (Fig. 2d). To explore the threshold at which the observed postsynaptic changes occur, we
138 calculated the $[^{11}\text{C}]$ raclopride/ $[^{11}\text{C}]$ DTBZ binding ratio for the right and left striatum. The ratio
139 remained close to 1 in the DPBS-injected striatum and control rats, indicating no substantial
140 difference between the two hemispheres. In contrast, VMAT2 knockdown rats displayed large
141 $[^{11}\text{C}]$ raclopride binding changes when the level of VMAT2 knockdown was ~ 20%. From this
142 point, a prominent increase in D2R binding was observed in the right striatum (Fig. 2e).
143 Therefore, this threshold was set to split the rats into *mild* (< 20%) and *moderate* (\geq 20%).
144 Notably, $[^{11}\text{C}]$ raclopride PET imaging was able to discriminate between different degrees of
145 synaptic dysfunction, classified from $[^{11}\text{C}]$ DTBZ binding changes (Fig. 2f).

146 We inspected the integrity of dopaminergic nerve terminals and the occurrence of
147 neuroinflammation in the striatum after the CRISPR/SaCas9-induced VMAT2 knockdown.
148 $[^{11}\text{C}]$ methylphenidate PET imaging of the dopamine transporter and $[^{18}\text{F}]$ GE-180 PET imaging of
149 the translocator protein, which is overexpressed on activated microglia, was performed.

150 CRISPR/SaCas9-induced VMAT2 knockdown did neither alter [¹¹C]methylphenidate binding, nor
151 [¹⁸F]GE-180 uptake (Fig. 2b,c).

152

153 **CRISPR/SaCas9-induced VMAT2 knockdown impairs motor function**

154 To explore the motor consequences of the CRISPR/SaCas9-induced VMAT2 knockdown, we
155 performed several behavioral tests (Fig. 3a).

156 We observed a reduction in the locomotor activity of VMAT2 knockdown rats in the open field test
157 (Fig. 3a), but no correlation to VMAT2 expression changes (Δ [¹¹C]DTBZ binding), or dopamine
158 availability (Δ [¹¹C]raclopride binding) (Supplementary Fig. 2a,b).

159 Next, we evaluated the forelimb akinesia using the cylinder test. VMAT2 knockdown rats
160 displayed a preference for the right forepaw, while control rats equivalently used their right and
161 left forepaw (Fig. 3c). Paw use alterations correlated highly with VMAT2 knockdown (Δ [¹¹C]DTBZ
162 binding), and dopamine availability (Δ [¹¹C]raclopride binding) (Fig. 3d,e).

163 To further examine differences in motor function, coordination, and balance, rats underwent the
164 beam walk test. VMAT2 knockdown rats stumbled with higher frequency to the left side, while
165 control rats displayed equal chances to slip in each direction (Fig. 3f). However, no correlations
166 between gait alterations and VMAT2 knockdown (Δ [¹¹C]DTBZ binding), or dopamine availability
167 (Δ [¹¹C]raclopride binding) were found (Supplementary Fig. 2c,d).

168 As previous studies suggest that body weight changes reflect striatal dopamine depletion [44], we
169 inspected the impact of the VMAT2 knockdown on the rats' body weight gain. VMAT2 knockdown
170 rats exhibited a 30% reduction in their gained weight over a period of 14 weeks, compared with
171 controls (Fig. 3g). Body weight gain correlated with changes in VMAT2 expression (Δ [¹¹C]DTBZ
172 binding), and dopamine availability (Δ [¹¹C]raclopride binding) (Fig. 3h,i).

173 To assess the rotational behavior, we performed the rotameter test with and without apomorphine
174 administration. In the spontaneous rotation test, VMAT2 knockdown rats displayed a higher
175 number of ipsilateral net turns compared with control rats (Fig. 3j). The number of turns did not

176 correlate with VMAT2 expression changes ($\Delta [{}^{11}\text{C}]\text{DTBZ}$ binding), and changes in dopamine
177 availability ($\Delta [{}^{11}\text{C}]\text{raclopride}$ binding) (Supplementary Fig. 2e,f). Apomorphine-induced rotations
178 to the contralateral side were higher in VMAT2 knockdown rats compared with control rats (Fig.
179 3k), and correlated with changes in VMAT2 expression ($\Delta [{}^{11}\text{C}]\text{DTBZ}$ binding) and dopamine
180 availability ($\Delta [{}^{11}\text{C}]\text{raclopride}$ binding) (Fig. 3l,m).

181
182 ***Ex vivo validation of the CRISPR/SaCas9-induced VMAT2 knockdown***
183 Using immunofluorescence, we confirmed the concomitant expression of SaCas9 and *Slc18a2*–
184 targeting sgRNA 19 weeks post-transduction, and a corresponding decrease of VMAT2
185 expression in the SNc of the VMAT2 knockdown group (Fig. 4b).

186 Immunohistochemistry revealed no changes in tyrosine hydroxylase (TH) expression levels in
187 striatum and SN in both groups (Fig. 4c,d), and confirmed the reduction of VMAT2 expression in
188 the right striatum and SN in the knockdown group (Fig. 4e).

189 Biochemical analysis showed a large reduction of dopamine, paralleled by an increased ratio of
190 metabolites (DOPAC, HVA) to dopamine, in the right striatum of VMAT2 knockdown rats (Fig.
191 4f,g). The reduced dopamine content correlated with the *in vivo* VMAT2 expression ($\Delta [{}^{11}\text{C}]\text{DTBZ}$
192 BP_{ND}) and postsynaptic changes ($\Delta [{}^{11}\text{C}]\text{RAC BP}_{\text{ND}}$) (Fig. 4h,i). Additionally, serotonin was
193 unchanged in the striata of VMAT2 knockdown and control rats, suggesting dopamine
194 nigrostriatal pathway specificity (Fig. 4j) (Metabolites' and neurotransmitters' striatal levels are
195 reported in Table 3).

196
197 ***Increased resting-state functional connectivity after CRISPR/SaCas9-induced VMAT2***
198 ***knockdown***

199 As multiple lines of evidence suggest a broader role of dopamine in the dynamic reconfiguration
200 of brain networks [17, 45, 46], we next investigated the impact of unilateral dopamine depletion
201 on brain rs-FC. A second cohort of rats underwent longitudinal simultaneous $[{}^{11}\text{C}]\text{raclopride}$ –

202 PET/BOLD-fMRI scans at baseline and 8 - 14 weeks after CRISPR/SaCas9-induced VMAT2
203 knockdown (Fig. 5a). [¹¹C]DTBZ PET scans and behavioral analysis confirmed previous findings
204 in the first cohort, that is, an efficient depletion of the VMAT2 (20% decrease of [¹¹C]DTBZ
205 binding) (Supplementary Fig. 3a), paralleled by motor disturbances in the cylinder test
206 (Supplementary Fig. 3e-g). In line with the findings of cohort 1, dopamine availability was
207 decreased (10% increase in [¹¹C]raclopride binding) and correlated to the extent of the VMAT2
208 knockdown (Supplementary Fig. 3b,c). An increase in D2R binding was observed in the right
209 striatum when the level of VMAT2 knockdown reached ~ 20% (Supplementary Fig. 3d), enabling
210 a subdivision into *mild* (< 20%) and *moderate* rats (≥ 20%).

211 We next assessed the occurrence of rs-FC changes in DMN and SMN. Our analysis focused on
212 identifying early biomarkers of *mild* dysfunction and patterns of spreading of synaptic dysfunction.
213 Figure 5b,c illustrates intraregional rs-FC group-level correlation matrices at baseline and after
214 VMAT2 knockdown in *mild* and *moderate* rats for the DMN and SMN, respectively. We observed
215 within-network rs-FC changes in rats with *moderate* VMAT2 knockdown, in both DMN and SMN.
216 Rats of the *mild* knockdown group revealed rs-FC changes up to 20%, in prefrontal cortical
217 regions of the DMN, and between the left thalamus (Th) and somatosensory cortex (SC) in the
218 SMN. However, these data need to be carefully interpreted as they did not survive a more
219 stringent *P* value selection (**P*< 0.01) (Supplementary Fig.4a,b) (*P* values are reported in
220 Supplementary Tables 1,3).

221 Rats with *moderate* VMAT2 knockdown exhibited a 60% increase in rs-FC within the right medial
222 prefrontal cortex (mPFC) and the right and left hippocampus (Hipp) (Fig. 5b) (*P* values are
223 reported in Supplementary Table 2).

224 FC increase between the left thalamus and somatosensory cortex in the SMN doubled to 34% in
225 rats with *moderate* VMAT2 knockdown and extended throughout the left and right thalamus and
226 striatum (STR), respectively (Fig. 5c) (*P* values are reported in Supplementary Table 4).

227 Moreover, we inspected rs-FC changes between the DMN and SMN at baseline and after the
228 CRISPR/SaCas9-induced VMAT2 knockdown.

229 Figure 5d illustrates internetwork rs-FC correlation matrices in rats with *mild* (left panel) and
230 *moderate* (right panel) VMAT2 knockdown. Brain graphs display the nodes and edges (raw
231 values) that demonstrated internetwork rs-FC changes to baseline (%). Strikingly, large
232 alterations between DMN and SMN were already observable in the *mild* VMAT2 knockdown
233 group. Rats presented opposite rs-FC changes between regions of the anterior/posterior DMN
234 and the SMN, compared with baseline. A 30 to 60% increase in rs-FC was observed between
235 regions of the anterior DMN and the SMN. Specifically, rs-FC increased between the right
236 orbitofrontal cortex (OFC) and striatum bilaterally and the contralateral somatosensory cortex,
237 and between the contralateral orbitofrontal cortex and striatum. Instead, a 20% decrease in rs-FC
238 was found between regions of the posterior DMN and the SMN. Specifically, rs-FC decreased
239 between the left retrosplenial cortex (RSC) and right somatosensory cortex (Fig. 5d, left panel) (*P*
240 values are reported in Supplementary Table 5).

241 Rats with a *moderate* VMAT2 knockdown presented increased rs-FC between regions of the
242 anterior/posterior DMN and the SMN, compared with baseline. Of particular note, internetwork rs-
243 FC changes were not found between the regions of the posterior DMN and the SMN that showed
244 decreased rs-FC in rats with *mild* VMAT2 knockdown. Moreover, between-network rs-FC
245 increase extended to other regions. A 60 to 80% increase in rs-FC was found between the medial
246 prefrontal cortex and the right striatum, and the motor (MC) and somatosensory cortex bilaterally.
247 FC increased by more than 20% between the hippocampi and contralateral somatosensory
248 cortex. (Fig. 5d, right panel) (*P* values are reported in Supplementary Table 6). Notably, between-
249 network rs-FC changes did not involve the thalamus, which connectivity was however altered
250 within the SMN.

251 Further, we examined how the rs-FC changes to baseline correlated between the *mild* and
252 *moderate* groups (Supplementary Fig. 5a). Group level intraregional and internetwork rs-FC

253 changes to baseline (%) correlated linearly between the two groups (Supplementary Fig. 5b-d).
254 Node correlation analysis indicated a linear increase in the magnitude of the rs-FC changes to
255 baseline in the hippocampi (Supplementary Fig. 5e), cingulate cortices (Supplementary Fig. 5f),
256 and contralateral, but not ipsilateral, thalamus (Supplementary Fig. 5g). Our data suggest a
257 similarity in the pattern of the intraregional and internetwork rs-FC changes between *mild* and
258 *moderate* VMAT2 knockdown rats and a linear relationship between the magnitude of the rs-FC
259 changes.

260 To complement the results of the intraregional and internetwork rs-FC, we evaluated changes in
261 regional mean connection distances. Network-wise graph theoretical analysis on node level was
262 paralleled by whole-brain connection-wise analysis to identify the nodes that were significantly
263 altered in rats with *mild* and *moderate* VMAT2 knockdown, compared with baseline, for the DMN
264 (Supplementary Fig. 6a,b) and SMN (Supplementary Fig. 6c,d). Briefly, the network organization
265 did not change in rats with *mild* VMAT2 knockdown, compared with baseline, as changes in the
266 global mean connection distance were not found in DMN (Supplementary Fig. 6a) nor SMN
267 (Supplementary Fig. 6c). Interestingly, in rats with *moderate* VMAT2 knockdown network
268 organization changes did not influence regions of the DMN (Supplementary Fig. 6b), but occurred
269 in the contralateral striatum and thalamus (Supplementary Fig. 6d) (*P* values are reported in
270 Supplementary Table 7).

271 Collectively, rs-FC results highlight lateralized effects in the SMN, as opposed to the symmetric
272 recruitment of DMN regions.

273

274 **CRISPR/SaCas9-induced VMAT2 knockdown alters GABA signaling**

275 Besides dopamine, dopaminergic neurons co-release GABA via the VMAT2 [47, 48]. To
276 investigate if GABA neurotransmission is altered following the VMAT2 knockdown, we performed
277 additional [¹¹C]flumazenil PET scans 10 – 12 weeks after the CRISPR/Cas9-editing, and

278 quantified the GABA-A binding in regions of the DMN and SMN (Fig. 6). In *mild* VMAT2
279 knockdown rats, we observed a decrease of [¹¹C]flumazenil binding in the ipsilateral parietal
280 cortex (PaC) (14%), hippocampus (4%), and somatosensory cortex (9%) (Fig. 6a,b). In *moderate*
281 VMAT2 knockdown rats we observed a decrease of [¹¹C]flumazenil binding in the ipsilateral
282 parietal cortex (11%), and somatosensory cortex (6%) (Fig. 6a,c). Our data indicate that
283 [¹¹C]flumazenil binding was altered regardless of the VMAT2 knockdown extent. This was further
284 evidenced by the lack of correlation between [¹¹C]DTBZ and [¹¹C]flumazenil binding changes in
285 the target regions (linear regression data not shown).

286

287 **Discussion**

288 Here, we show the potential of combining CRISPR/Cas9 gene-editing with molecular and
289 functional brain imaging to identify early adaptations of brain circuits in response to targeted gene
290 and protein modulations. Using CRISPR/SaCas9, we knocked down the *Slc18a2* gene, encoding
291 the VMAT2, which plays a key role in the storage and release of dopamine in response to
292 neuronal activity [43]. The CRISPR-mediated knockdown allowed us to investigate the VMAT2-
293 dependent dopamine signaling in the striatum, while structurally preserving neuronal integrity.
294 [¹⁸F]GE-180 results suggest that glial activation is not the source of dopaminergic synaptic
295 dysfunction, and exclude the occurrence of inflammatory responses arising from the surgical
296 procedure and the chosen AAV-serotype, which could influence our readout, in line with recent
297 reports [49]. Our data reveal that the targeted gene knockdown in the SNC leads to an expected
298 reduction of dopamine release in the striatum, paralleled by [¹¹C]raclopride binding changes. It is
299 conceivable that the observed postsynaptic changes are the result of an increase in binding due
300 to the reduced dopamine concentration in the striatum. Yet, several studies have revised this
301 notion [50, 51]. In this regard, our results of the drug-evoked rotational behavior are in better
302 agreement with a D2R compensatory upregulation. Indeed, supersensitivity to apomorphine in
303 rats with nigrostriatal lesions or VMAT2 knockout is accompanied by an increase in striatal D2R

304 binding sites, but no change in affinity [52-57]. Further, the observed striatal increase in
305 [¹¹C]raclopride binding is independent of presynaptic nerve terminal loss and occurs in response
306 to a ~ 20% decrease of [¹¹C]DTBZ binding. This confirms, in line with our [¹¹C]methylphenidate
307 results, that [¹¹C]raclopride can be used to delineate postsynaptic changes in the absence of
308 dopamine transporter-mediated compensation, triggered by neuronal loss. Accordingly, increased
309 [¹¹C]raclopride binding is observed in the early but not later stages of Parkinson's disease [58],
310 characterized by severe neuronal cell loss, and dopamine transporter changes (> 50%) [59].
311 Consistently, rats with severe denervation (> 75%) present earlier mitigation by the dopamine
312 transporter, followed by D2R binding changes [60]. Hence, with our method, it is feasible to study
313 the consequences of synaptic dopamine dysfunction without compensations triggered by
314 neuronal cell loss. Moreover, the observed [¹¹C]raclopride and [¹¹C]DTBZ correlations to the
315 motor behavior highlight that [¹¹C]raclopride binding remains at control levels as long as synaptic
316 dopamine levels are sufficient to maintain adequate motor function. Motor disturbances strongly
317 correlate to pre and postsynaptic changes if movements of the forelimbs, but not whole-body, are
318 considered, in agreement with earlier observations in dopamine-depleted rats [44]. Depletion of
319 VMAT2 resulted in reduced dopamine tissue levels in the ipsilateral striatum, nicely merging with
320 the *in vivo* data. Moreover, metabolite analysis suggested that due to the lack of VMAT2-
321 mediated storage in presynaptic vesicles, dopamine is quickly converted. The increased
322 metabolism might as well be a possible compensatory mechanism consequent to the VMAT2
323 knockdown, reflecting actions that residual nigrostriatal neurons undertake to maintain dopamine
324 homeostasis, as already speculated by others [53, 61].
325 To elucidate the role of VMAT2 in locomotion, reward, and Parkinson's disease, several
326 investigators have deleted its coding gene in mice [62-65]. Besides the costly and time-
327 consuming breeding, the gene knockout was not selective for dopaminergic neurons, resulting in
328 the appearance of anxiety and depressive behavior phenotypes [66]. CRISPR/Cas9-editing
329 overcomes these limitations, allowing gene-editing in adult and aged animals and avoiding

330 compensatory changes occurring at early developmental stages. Since its discovery, only two
331 studies have successfully applied CRISPR/Cas9 in the rat brain [40, 67], where gene-editing has
332 been difficult to adapt. Rats are particularly advantageous for imaging studies due to the larger
333 brain size and limited spatial resolution and sensitivity of preclinical scanners [68]. Here, by
334 inducing a *mild* to *moderate* gene knockdown, we could investigate early to late resting-state
335 brain network adaptations prompted by presynaptic dysfunction. We show that the selective
336 impairment of presynaptic dopamine storage and release is followed by rs-FC alterations within
337 and between the DMN and SMN. Our results confirm previous findings that the DMN, associated
338 with ideation and mind wandering [69], and the SMN, involved in sensory processing and motor
339 function [70], do not function in isolation from each other, but rather synchronize [71]. The
340 observed internetwork synchronization may reflect compensatory brain reorganization, as already
341 speculated by others [72, 73]. We also identified enhanced intranetwork rs-FC in the DMN and
342 SMN. Rs-FC changes were observed in prefrontal cortical regions, hippocampus, thalamus, and
343 striatum. Our data parallel previous findings of cortico-striato-thalamic hyperconnectivity in
344 decreased dopamine transmission states [74-77]. In line, increased synchronous neural
345 oscillatory activity and functional coupling in the basal ganglia and its associated networks have
346 been observed in Parkinson's disease [78-83]. The increase of cortico-striatal FC could in part be
347 due to dysfunctions of multiple tonic inhibitory gate actions of D2R [84]. Increased FC across the
348 thalamus and prefrontal cortex has been reported in drug-treated Parkinson's disease patients
349 [85, 86], potentially indicating functional compensation, as the brain recruits additional anatomical
350 areas to aid in restoring cognitive processes. This might as well explain the engagement of the
351 hippocampus, functionally connected with DMN cortical regions [87, 88]. In this regard, research
352 has shown that the hyperconnectivity of brain circuits is a common response to neurological
353 dysfunction, and may reflect a protective mechanism to maintain normal brain functioning [89].
354 Such a mechanism has been proposed in Parkinson's disease, mild cognitive impairment, and
355 Alzheimer's disease [90-93]. Collectively, our findings support this model and indicate a

356 reorganization of brain networks that adapt to the synaptic dysfunction through enhanced
357 interregional synchrony. Recruiting alternative brain regions may be an early response to the
358 dysfunction preceding neuronal cell loss and motor impairment. Interestingly, brain connectome
359 adaptations occurred symmetrically in the DMN but were more weighted towards the contralateral
360 hemisphere in the SMN.

361 Besides dopamine, dopaminergic neurons co-release GABA via the VMAT2. This hints towards
362 reduced GABA following the VMAT2 knockdown, and consequent imbalance in downstream
363 striatal projection neurons of the direct and indirect pathway [47, 48, 94]. GABA regulates the
364 inhibitory neurotransmission in various brain areas through GABA-A receptors [95]. We
365 hypothesize that decreased binding to the GABA-A receptors may be consistent with loss of
366 inhibitory tone in multiple cortical areas, reflected by our $[^{11}\text{C}]$ flumazenil PET data, resulting in
367 increased localized brain connectivity, reflected in the fMRI signal. The suppression of the
368 GABAergic feedback circuit, mediated by D2R and external globus pallidus neurons [84],
369 complements the observed elevation in neuronal synchronicity. Our postulation is in line with
370 earlier findings of an inverse correlation of GABA with rs-FC in DMN [96] and with a putative role
371 of loss of inhibitory tone in hyperconnectivity [97]. Interestingly, our $[^{11}\text{C}]$ flumazenil PET data did
372 not reveal changes in GABA-A expression in the striatum. Instead, we observed a significant
373 decrease in the ipsilateral hemisphere of several cortical regions in both *mild* and *moderate* rats,
374 supporting previous findings of GABA modulation of the internetwork FC [98]. Studies report
375 downregulated inhibitory neurotransmission in Parkinson's disease, where gene expression of
376 GABAergic markers is low in the frontal cortex [99, 100]. Further, inverse correlations between
377 $[^{11}\text{C}]$ flumazenil binding and gait disturbances [101], and between GABA concentration in the
378 motor cortex and disease severity have been reported [102]. Moreover, our $[^{11}\text{C}]$ flumazenil PET
379 results suggest that GABA neurotransmission is disturbed already at the *mild* stage, indicating its
380 potential role as an early biomarker of dopaminergic presynaptic dysfunction. Of note, the
381 observed changes in GABA-A binding might indicate only an apparent decrease in binding due to

382 the reduced GABA availability, or reflect compensatory adaptation on the contralateral
383 hemisphere. Future research should elucidate these aspects and also perform further
384 investigations on glutamate, due to the crucial role of the excitatory/inhibitory-imbalance in
385 several psychiatric disorders [103].

386

387 **Limitations and general remarks**

388 We knocked down VMAT2 in dopaminergic projection neurons from the SNC to the dorsal
389 striatum. To achieve selective targeting of this neuronal subtype, rat Cre driver lines have been
390 developed [67, 104]. Although all monoamine-releasing neurons express VMAT2, in contrast to
391 other brain regions, SNC neurons are predominantly dopaminergic [105]. Thus, even though we
392 used wild-type rats, we can largely dismiss effects on other monoaminergic neurons, as also
393 indicated by biochemical analysis of serotonin striatal levels.

394 Despite its limited off-target editing [38], undesired targeting of SaCas9 on other genes cannot be
395 fully excluded. Nevertheless, off-target candidates with up to 4 mismatches were screened in the
396 whole genome of *Rattus norvegicus* (<http://www.rgenome.net/cas-offinder/>), consistently with
397 past reports [40]. To the best of our knowledge, the off-target matches (*Ndrg1*, *RGD1305938*,
398 *Btn2a2*, *AABR07042293.2*) have no effects on VMAT2 function, being involved in cell
399 differentiation, T-cell regulation, and mRNA processing, respectively
400 (<https://www.ncbi.nlm.nih.gov/IEB/Research/Acembly/index.html>).

401 Another limitation of the study is the relatively small sample size, related to the complex and high-
402 cost procedures involved in the *in vivo* imaging measurements. In addition to this, the intrinsically
403 high intersubject variability in rs-fMRI, and differences in knockdown efficiency contributed to
404 significant variance in our cohorts. Nevertheless, the variability of gene-editing efficiency was in
405 line with previous *in vivo* brain studies [40, 41].

406

407 **Conclusions**

408 This work encourages the combinatorial use of CRISPR/Cas9 and molecular and functional *in*
409 *vivo* brain imaging to achieve selective modulation of genes and understand the related functional
410 adaptations in brain networks, beyond the targeted circuitry.

411 We anticipate our approach to be a starting point to shed the light on the function of specific
412 genes and their encoded proteins on whole-brain connectivity, useful to understand the cellular
413 basis of functional changes, identify early neurobiological markers, and promising therapeutic
414 interventions.

415

416 **Methods**

417 **Animals**

418 Female wild-type Long Evans rats (224 ± 30 g, $n = 57$) (Charles River Laboratories, Sulzfeld,
419 Germany) were kept on a 12 h day-night cycle at a room temperature of 22 °C and 40 - 60%
420 humidity. Animals received a standard diet and tap water *ad libitum* before and during the
421 experimental period. All animal experiments were performed according to the German Animal
422 Welfare Act and were approved by the local ethical authorities, permit numbers R15/19M,
423 R4/20G.

424

425 **Viral vectors**

426 SgRNAs targeting the second exon of the *Slc18a2* gene and the first exon of the *lacZ* gene were
427 designed based on the PAM sequence of SaCas9 (NNGRRT) (Table 1). SgRNAs were cloned
428 into an AAV-PHP.EB expression vector containing a GFP reporter sequence, driven by the CMV
429 promoter, for the identification of transduced neurons. A second AAV-PHP.EB construct was
430 produced to express SaCas9, flanked by two nuclear localization sequences (NLS) to allow its
431 translocation into the nuclei. The vector expressed the nuclease via the CAG promoter and
432 contains three HA-tags to visualize the targeted neurons (Fig. 1a). Cloning of the sgRNAs,
433 plasmid construction, as well as the production of concentrated and purified AAV-PHP.EB
434 vectors, delivered at a concentration of 10^{13} gc/mL, were carried by SignaGen Laboratories
435 (Johns Hopkins University, USA). A European patent application has been filed for the AAV-
436 PHP.EB vectors and is currently pending.

437 The genomic mutation rate was assessed using a different set of AAVs with AAV2/1 serotype, for
438 a conditional design, kindly provided by Matthias Heidenreich (prev. Zhang lab, Broad Institute of
439 MIT and Harvard, Cambridge, USA).

440

441 **Rat primary cortical neuron culture**

442 Primary cortical neurons were obtained from rat embryos of a pregnant Sprague Dawley rat from
443 embryonic day 18 (E18) (Charles River, Sulzfeld, Germany). Embryos were decapitated and
444 quickly removed from the mother rat. Cortical dissection was performed in ice-cold HBSS
445 (100 mL 10 × HBSS, 870 mL dH₂O, 3.3% 0.3 M HEPES pH 7.3 and 1% pen/strep)
446 (LifeTechnologies, Massachusetts, USA). The obtained tissue was washed three times with
447 10 mL ice-cold HBSS PhenolRed-free (LifeTechnologies, Massachusetts, USA) and then
448 digested at 37 °C for 20 min in 8 mL HBSS with 2.5% trypsin (LifeTechnologies, Massachusetts,
449 USA). Cortices were washed 3 times with 10 mL HBSS containing 3.7% FBS, and then gently
450 triturated in 2 mL HBSS. For the maintenance, neurons were plated on poly-D-lysine-coated 24
451 well plates (BD Biosciences, Heidelberg, Germany) or coverslips (Neuvitro Corporation,
452 Vancouver, USA) at a density of 16 × 10⁴/well, and cultured in Neurobasal media supplemented
453 with 2% 1 × B27, 0.25% Glutamax, 0.125% Glutamate and 1% pen/strep (LifeTechnologies,
454 Massachusetts, USA) for four days. Afterward, for the immunofluorescence, AAVs carrying the
455 expression of the vectors for the SaCas9 and sgRNAs (1:1 ratio), were added to the culture
456 medium at 200,000 MOI (AAV-PHP.EB-sgRNA-*lacZ*: 1.7 × 10¹² gc/mL, AVV-PHP.EB-SaCas9:
457 1.4 × 10¹² gc/mL, AAV-PHP.EB-sgRNA-*Slc18a2*: 2.1 × 10¹² gc/mL, final viral volume
458 37.5 µL/well). For the Surveyor assay, conditional AAVs for SaCas9, sgRNA-*Slc18a2*, Cre-
459 recombinase (AAV2/1, 1:1:0.5 ratio) were used. Neurons were processed 1-week post-viral
460 treatment (Fig. 1b).

461

462 **Surveyor assay**

463 To estimate the VMAT2 knockdown efficiency of the designed sgRNA *in vitro*, we evaluated the
464 presence of genetic deletions in rat primary neurons with the Surveyor assay (Surveyor kit,
465 Integrated DNA Technologies, Coralville, USA). One week following the viral infection, the

466 genomic DNA was extracted using the QuickExtract DNA Extraction solution (Epicentre,
467 Madison, USA), according to the manufacturer's instructions, and was normalized to 100 ng in
468 dH₂O. 18 - 25 nt primers were designed 200 - 400 bp away from either side of the SaCas9 target
469 site to amplify the loci of interest by touchdown PCR (oligonucleotides used for PCR are provided
470 in Supplementary Table 8). DNA amplification was performed using 0.5 µL Phusion Polymerase
471 (LifeTechologies, Massachusetts, USA), as previously reported [106]. A single band product was
472 visualized on 1.5% agarose gel, isolated, and purified using QIAquick Spin columns (Qiagen,
473 Hilden, Germany), following the supplier's protocol. 400 ng of the purified PCR product were
474 mixed with 2 µL Taq DNA polymerase buffer (LifeTechologies, Massachusetts, USA) to allow
475 the cross-annealing of the mutated and wild-type sequences. The re-annealing process was
476 conducted at the following cycling conditions: 10 min at 95 °C, 95 °C to 85 °C at -2 °C/s, hold
477 1 min, ramp down to 75 °C at -0.3 °C/s, hold 1 min, and so on until 25 °C temperature was
478 reached. Samples were then stored at 4 °C. This cross-annealing procedure converts the
479 mutations into mismatch duplexes (heteroduplexes), which can be recognized by performing
480 nuclease digestion [107]. We digested the annealed products for 20 min at 42 °C using 2.5 µL
481 MgCl₂ (0.15 M), 1 µL Surveyor nuclease, and 1 µL Surveyor enhancer. Digested products were
482 then resolved on a 2.5% agarose gel, stained with 0.01% SYBR Gold DNA (LifeTechologies,
483 Massachusetts, USA) in 1% TBE buffer. The size of the occurring bands indicated the location of
484 the mutation (expected DNA fragments sizes are provided in Supplementary Table 8). To
485 quantify the knockdown efficiency, the software ImageJ was used. Peak areas of the bands
486 visualized on agarose gel were selected and the percentages of the transduced neurons
487 acquiring the InDel mutation were calculated using the following formula [106]:

$$Editing (\%) = 100 \times \left(1 - \sqrt{\left(1 - \frac{b+c}{a+b+c}\right)}\right)$$

488 where a is the integrated intensity of the undigested PCR product and b and c are the integrated
489 intensities of each cleavage fragment from the digested product.

490

491 **Immunofluorescence of rat primary neurons**

492 Rat primary neurons were processed 1-week post-AAV-transduction. Coverslips were washed
493 twice with DPBS and fixed in 4% PFA in DPBS for 15 min at room temperature. Blocking and
494 permeabilization were performed for 30 min in DPBS with 5% donkey serum, 0.5% Triton-X100,
495 and 0.05% BSA. Primary antibody incubation (VMAT2, 1:50, EB06558, Everest Biotech,
496 Ramona, USA, HA-tag: 1:50, 682404, Biolegend, San Diego, USA) was performed for 60 min,
497 followed by Cy3 conjugated secondary antibody incubation (1:250, kindly provided from Birgit
498 Fehrenbacher, Department of Dermatology, University of Tuebingen, Germany). Coverslips were
499 mounted using ProLong Antifade Diamond Medium containing DAPI (LifeTechnologies,
500 Massachusetts, USA), and imaged with a TCS-SP2/Leica DM IRE2 confocal laser scanning
501 microscope. Images were processed with Leica Confocal Software LCS (Version 2.61) (original
502 magnification 630) (Leica Microsystems, Wetzlar, Germany).

503

504 **Study design of the *in vivo* experiments**

505 In a first cohort, AAVs-CRISPR/SaCas9 were stereotactically delivered into the right SNc of wild-
506 type rats. Afterward, *in vivo* PET scans with imaging markers of VMAT2 expression, dopamine
507 availability, nerve terminal integrity, and inflammatory responses were performed in VMAT2
508 knockdown and control rats using [¹¹C]DTBZ, [¹¹C]raclopride, [¹¹C]methylphenidate, and [¹⁸F]GE-
509 180, respectively. Motor consequences of the CRISPR/SaCas9-induced VMAT2 knockdown
510 were explored in a wide spectrum of behavioral tasks. Finally, biochemical and histological
511 analyses were performed to corroborate the *in vivo* data (Fig. 2,3,4a).

512 In a second cohort, cylinder test and [¹¹C]raclopride-PET/BOLD-fMRI scans were performed at
513 baseline and after CRISPR/SaCas9-induced VMAT2 knockdown. These measurements were
514 paralleled by *in vivo* PET scans with imaging markers of VMAT2 and GABA-A expression, to

515 inspect the extent of the induced VMAT2 knockdown and its impact on GABA signaling, using
516 [¹¹C]DTBZ and [¹¹C]flumazenil, respectively (Fig. 5a).

517

518 **Stereotactic injections**

519 Rats were anesthetized by injecting a mixture (1 mL/kg) of fentanyl (0.005 mg/kg), midazolam
520 (2 mg/kg,) and medetomidine (0.15 mg/kg) intraperitoneally, and were placed onto a stereotactic
521 frame (Harvard Apparatus, Holliston, MA, USA) with the skull flat between Lambda and Bregma.
522 The following coordinates were used for the injections (flat skull position): AP: - 5 mm, ML:
523 \pm 2 mm, DV: - 7.2 mm, below the dural surface as calculated relative to Bregma. Rats were
524 injected with 3 μ L AAVs into the right SNC and were divided into two groups. Control rats (n= 10)
525 were injected with AAV-PHP.EB-sgRNA-*lacZ* (1.7×10^{12} gc/mL) and AVV-PHP.EB-SaCas9
526 (1.4×10^{12} gc/mL) (1:1 ratio). VMAT2 knockdown rats (n= 47) were injected with AAV-PHP.EB-
527 sgRNA-*S/c18a2* (2.1×10^{12} gc/mL) and AVV-PHP.EB-SaCas9 (1.4×10^{12} gc/mL) (1:1 ratio) (see
528 Fig. 1a for vector constructs). DPBS (3 μ L) was sham-injected into the contralateral SNC.
529 Solutions were infused at a rate of 0.2 μ L/min using a 5 μ L Hamilton syringe (Hamilton, Bonaduz,
530 Switzerland) and an automated microsyringe pump (Harvard Apparatus, Holliston, MA, USA). To
531 allow for the diffusion of AAVs into the tissue, the needle was left in place for 10 min, and then
532 slowly retracted at 0.2 mm/min. After the surgery, an antidote containing atipamezole
533 (0.75 mg/kg) and flumazenil (0.2 mg/kg) was injected subcutaneously. The rats were kept warm
534 in their cages until fully recovered.

535

536 **Radiotracer synthesis**

537 [¹¹C]CO₂ was produced on a medical cyclotron (PETtrace 860, GE Healthcare, Uppsala,
538 Sweden) using the ¹⁴N(p, α)¹¹C route and converted to either [¹¹C]MeI (methyl iodide) or
539 [¹¹C]MeOTf (methyl triflate) using a Tracerlab FX MeI module (GE Healthcare). A Tracerlab FX M

540 module (GE Healthcare) was used for automated methylation, purification, and formulation of the
541 tracers.

542 [¹¹C]Dihydrotetrabenazine (DTBZ), a VMAT2 ligand, was synthesized starting from [¹¹C]MeI,
543 which was reacted with 1 mg (+)-9-O-desmethyl-dihydrotetrabenazine (ABX, Radeberg,
544 Germany) in 300 μ l DMF in the presence of 7.5 μ l 5 M NaOH for 3 min at 40 °C [108]. Afterward,
545 it was purified by HPLC and formulated as a sterile pyrogen-free saline solution. The total
546 synthesis time from the end of the beam was 45 min. The radiochemical purity of the final
547 radiotracer was > 95% as determined by HPLC. Molar activity at the time of injection was 96 ± 37
548 GBq/ μ mol.

549 D-threo-[¹¹C]methylphenidate, a dopamine transporter ligand, was synthesized by alkylation of D-
550 threo-N-NPS-ritalinic acid (ABX) using [¹¹C]MeI [109]. After acidic deprotection, purification, and
551 formulation, the product was obtained with a 37 ± 6% decay-corrected radiochemical yield (from
552 [¹¹C]MeI). The total synthesis time was 55 min, and the radiochemical purity of the final
553 formulated radiotracer was > 95% as determined by HPLC analysis. The molar activity was
554 determined at the time of injection as 58 ± 14 GBq/ μ mol.

555 [¹¹C]Raclopride a D2R ligand, was synthesized by alkylation of S-(+)-O-desmethyl-raclopride
556 (ABX) using [¹¹C]MeOTf. After purification and formulation, the product was obtained with a
557 12 ± 4% decay-corrected radiochemical yield (from [¹¹C]methyl triflate). The total synthesis time
558 from the end of the beam was 55 min. The radiochemical purity of the final formulated radiotracer
559 was > 95% as determined by HPLC. The molar activity was determined at the time of injection
560 and was calculated as 88 ± 41 GBq/ μ mol.

561 [¹¹C]Flumazenil, a GABA-A ligand, was synthesized by methylation of desmethylflumazenil (ABX)
562 with [¹¹C]MeI. 2 mg of the precursor were dissolved in 0.3 ml DMF with 3 μ l 5 M NaOH and
563 reacted for 2 min at 80 °C. After the reaction, the product was purified by semi-preparative HPLC

564 and reformulated by solid-phase extraction (Strata-X, Phenomenex; elution with 0.5 ml ethanol,
565 dilution with 5 ml phosphate-buffered saline). The total synthesis time from the end of the beam
566 was 50 min. The radiochemical purity of the final formulated radiotracer was > 95% as
567 determined by HPLC. The molar activity was determined at the time of injection as
568 109.5 ± 39.6 GBq/ μ mol.

569 $[^{18}\text{F}]$ Fluoride was produced on a PETtrace 860 medical cyclotron (GE Healthcare) using
570 the $^{18}\text{O}(\text{p},\text{n})^{18}\text{F}$ route.

571 $[^{18}\text{F}]$ GE-180, a translocator protein ligand [110], was synthesized on a FASTlab synthesizer (GE
572 Healthcare) with precursor and reagent kits in single-use cassettes (GE Healthcare) according to
573 the manufacturer's instructions. The radiochemical purity of the final formulated radiotracer was
574 > 95% as determined by HPLC. The molar activity was determined at the time of injection as
575 576 ± 283 GBq/ μ mol.

576

577 ***In vivo* PET imaging and data analysis**

578 For the study of cohort 1, VMAT2 knockdown (n= 14) and control rats (n= 10) underwent 60 min
579 dynamic PET emission scans with $[^{11}\text{C}]$ DTBZ (8 – 10 weeks post-injection), $[^{11}\text{C}]$ methylphenidate
580 (10 – 12 weeks post-injection), $[^{11}\text{C}]$ raclopride (12 – 14 weeks post-injection) and $[^{18}\text{F}]$ GE-180
581 (14 – 16 weeks post-injection) (Fig. 2a). Four rats were excluded from the data analyses because
582 two rats from each group died during a PET acquisition. One control rat was excluded from the
583 $[^{11}\text{C}]$ methylphenidate analysis due to a poor signal-to-noise ratio.

584 For the study of cohort 2, VMAT2 knockdown rats (n= 33), underwent 60 min dynamic PET
585 emission acquisitions with $[^{11}\text{C}]$ DTBZ (8 – 10 weeks post-injection), and $[^{11}\text{C}]$ flumazenil (10 –
586 12 weeks post-injection). The final cohort included 23 rats (see paragraph Simultaneous
587 PET/fMRI experiments).

588 Three small-animal PET scanners (Inveon, Siemens, Erlangen, Germany) and dedicated rat
589 brain beds (Jomatik GmbH, Tuebingen, Germany) with stereotactic holders and temperature
590 feedback control units (Medres, Cologne, Germany) were used. These ensured the delivery and
591 removal of the anesthesia gas and stabilized the body temperature at 37 °C during the PET data
592 acquisition. Anesthesia was induced by placing the animals in knock-out boxes and delivering 2%
593 isoflurane in oxygen air. Subsequently, a 24 G catheter (BD Insyte, NJ, USA) was placed into the
594 tail vein for the tracer and/or *i.v.* anesthesia administration. Afterward, animals of cohort 1 were
595 anesthetized with 2% isoflurane vaporized in 1.0 L/min of oxygen. Animals of cohort 2 received a
596 medetomidine bolus injection (0.05 mg/kg) and the anesthesia was switched to constant
597 medetomidine infusion (0.1 mg/kg/h), and 0.5% isoflurane in air during the scan time, as adapted
598 from the literature [111].

599 The rats were placed in the center of the field of view and PET acquisitions started 5 s before the
600 bolus injection of the tracer. In Supplementary Tables 9 and 10, injected activity (MBq/kg) and
601 molar activity (GBq/μmol) at the time of injection are reported for each radioligand. The list-mode
602 data from the dynamic acquisitions of [¹¹C]DTBZ, [¹¹C]raclopride, [¹¹C]methylphenidate, and
603 [¹¹C]flumazenil were histogrammed into 39 time-frames (12x5 s, 6x10 s, 6x30 s, 5x60 s,
604 10x300 s), from [¹⁸F]GE-180 into 16 time-frames (5x60 s, 5x120 s, 3x300 s, 3x600 s). PET scans
605 of the study cohort 1 were reconstructed using the OSEM3D map algorithm, and a matrix size of
606 256 x 256 x 159, resulting in a pixel size of 0.38 x 0.38 x 0.79 mm. PET scans of the study cohort
607 2 were reconstructed using the OSEM2D algorithm, and a matrix size of 256 x 256 x 89, resulting
608 in a pixel size of 0.33 x 0.33 x 0.79 mm.

609 Data preprocessing analysis was performed with Matlab (Mathworks, Natick, MA, USA),
610 Statistical Parametric Mapping 12 (SPM12, Wellcome Trust Centre for Neuroimaging, University
611 College London, England), and the QModeling toolbox [112]. First, realignment of all frames was
612 performed using SPM12 and average images were generated for every scan. The mean images
613 were then used for coregistration to the Schiffer rat brain atlas provided by PMOD software [113].

614 To generate the respective time activity curves (TAC), volumes of interest (VOIs) were defined
615 over the target and reference regions. VOIs were placed over the right and left striatum for
616 [¹¹C]DTBZ, [¹¹C]raclopride, and [¹¹C]methylphenidate, and over the regions reported in Table 2 for
617 [¹¹C]flumazenil. Cerebellum was used as reference region for [¹¹C]DTBZ, [¹¹C]raclopride and
618 [¹¹C]methylphenidate. Pons was used as reference region for [¹¹C]flumazenil.

619 Binding potentials for [¹¹C]DTBZ, [¹¹C]raclopride, [¹¹C]methylphenidate and [¹¹C]flumazenil were
620 calculated over the all frames in the regions of interest with Logan reference [114], with a
621 population average k2' ([¹¹C]DTBZ: 0.41 min⁻¹, [¹¹C]raclopride: 0.34 min⁻¹, [¹¹C]methylphenidate:
622 0.18 min⁻¹, [¹¹C]flumazenil: 0.27 min⁻¹). [¹¹C]DTBZ and [¹¹C]raclopride binding changes (%), here
623 expressed as Δ binding, were calculated according to the formula:

$$\Delta \text{binding} = \frac{1 - \text{binding right striatum}}{\text{binding left striatum}} \times 100$$

624 [¹⁸F]GE-180 uptake in the right striatum was calculated over the interval between 30 – 60 min
625 after scan start and normalized by the uptake calculated in the left (DPBS-injected) striatum over
626 the same time interval.

627 QModeling was used to generate voxel-wise binding potential maps for [¹¹C]DTBZ,
628 [¹¹C]raclopride, [¹¹C]methylphenidate, and [¹¹C]flumazenil. [¹⁸F]GE-180 average uptake images
629 were generated with an in-house-written script in MATLAB.

630

631 **Simultaneous PET/fMRI experiments**

632 Rats (n= 33) underwent longitudinal simultaneous [¹¹C]raclopride-PET/BOLD-fMRI scans at
633 baseline and 8 – 14 weeks after CRISPR/SaCas9-induced VMAT2 knockdown. Three rats had to
634 be excluded from the data analyses due to aliasing artifacts, local distortion, and motion during
635 the data acquisition. Seven rats died during a PET/BOLD-fMRI scan. The final cohort included 23

636 rats. Anesthesia induction and injection were performed as described above for the cohort 2 (see
637 paragraph *In vivo* PET imaging and data analysis).

638 Next, rats were placed onto a dedicated rat bed (Medres, Cologne, Germany) and a temperature
639 feedback control unit (Medres, Cologne, Germany), ensuring the delivery and removal of the
640 anesthesia gas and stabilizing the body temperature at 37 °C during the scan time. A breathing
641 pad and a pulse oximeter were used to observe respiration and heart rates. Scans were acquired
642 using a small-animal 7 T Clinscan MRI scanner, a 72 cm diameter linearly polarized RF coil
643 (Bruker) for transmission, and a four-channel rat brain coil for reception (Bruker Biospin MRI,
644 Ettlingen, Germany). Localizer scans were first acquired to accurately position the rat brains into
645 the center of the PET/MRI field of view. Subsequently, local field homogeneity was optimized by
646 measuring local magnetic field maps. Anatomical reference scans were performed using T2-
647 weighted Turbo-RARE MRI sequences (TR: 1800 ms, TE: 67.11 ms, FOV: 40 x 32 x 32 mm,
648 image size: 160 x 128 x 128 px, Rare factor: 28, averages: 1). Finally, T2*-weighted gradient
649 echo EPI sequences (TR: 2500 ms, TE: 18 ms, 0.25 mm isotropic resolution, FoV 25 x 23 mm,
650 image size: 92 x 85 x 20 px, slice thickness 0.8 mm, slice separation 0.2 mm, 20 slices) were
651 acquired for BOLD-fMRI.

652 A dedicated small-animal PET insert developed in cooperation with Bruker (Bruker Biospin MRI,
653 Ettlingen, Germany) was used for the [¹¹C]raclopride acquisitions, the second generation of a
654 PET insert developed in-house with similar technical specifications [115]. [¹¹C]Raclopride was
655 applied via a bolus injection. In Supplementary Table 10 injected activities (MBq/kg) and molar
656 activities (GBq/μmol) at the time of injection are reported. PET/fMRI acquisitions started
657 simultaneously with the tracer injection and were performed over a period of 60 min. The list-
658 mode files of the PET data were histogrammed into 14 time-frames (1x30 s, 5x60 s, 5x300 s,
659 3x600 s), the 30s between acquisition start and the injection were excluded from the analysis.
660 Reconstruction was performed with an in-house-written OSEM2D algorithm. Data preprocessing
661 and analysis were performed as described above (see paragraph *In vivo* PET imaging and data

662 analysis). A population average $k2'$ ($[^{11}\text{C}]\text{raclopride}$ baseline: 0.20 min^{-1} , $[^{11}\text{C}]\text{raclopride}$ VMAT2
663 knockdown: 0.23 min^{-1}) was set for the Logan reference [114].

664 Preprocessing of the fMRI data was performed using a pipeline employing SPM12, Analysis of
665 Functional NeuroImages (AFNI, National Institute of Mental Health (NIMH), Bethesda, Maryland,
666 USA), and in-house-written scripts in MATLAB, as reported previously [116].

667 RS-FC was calculated using a seed-based approach. To this extent, 20 regions were selected
668 from the Schiffer rat brain atlas (a list of the regions is provided in Table 2). The SPM toolbox
669 Marseille Boîte À Région d'Intérêt (MarsBaR) was employed to extract fMRI time-courses from all
670 regions [117]. These were then used to calculate pairwise Pearson's r correlation coefficients for
671 each dataset, generating correlation matrices containing 20×20 elements. Self-correlations were
672 set to zero. The computed Pearson's r coefficients then underwent Fischer's transformation into z
673 values for group-level analysis.

674 Several rs-FC metrics were computed on different regional levels to investigate the potential
675 effects of dopamine depletion in the right striatum. Regional node strengths were computed as
676 the sum of all correlations of one seed to the regions included in one network. Interregional node
677 strengths were defined as the sum of the correlations of one node to the regions of another
678 network. Network strengths were defined as the sum of strengths of all correlations between
679 regions belonging to a network. Internetwork strengths were calculated as the sum of all
680 correlations between two sets of regions belonging to two networks [118].

681

682 **Behavioral analysis**

683 *Cylinder test*

684 Untrained rats were placed individually inside a glass cylinder (19 cm Ø, 20 cm height). The test
685 started immediately and lasted 5 min. During the test session rats were left undisturbed and were
686 videotaped with a camera located at the bottom-center of the cylinder to allow a 360° angle view.

687 Paw touches were analyzed using a slow-motion video player (VLC software, VideoLan). The

688 number of wall touches, contacts with fully extended digits, was counted. Data were analyzed as
689 follows:

$$\text{contralateral paw touches (\% to total)} = \frac{\text{contralateral touches}}{\text{total touches}} \times 100$$

690 One rat from the cohort 2 was excluded from the analysis due to issues during video recording.

691

692 *Rotameter test*

693 Rotational asymmetry was assessed using an automated rotameter system composed of four
694 hemispheres (TSE Systems GmbH, Bad Homburg, Germany) based on the design of Ungerstedt
695 and Arbuthnott [119]. Rats were placed into an opaque half bowl (49 cm Ø; 44 cm height) and
696 fixed to a moveable wire with a collar. The number of clockwise (CW) and counterclockwise
697 (CCW) rotations (difference of 42.3° in their position) were automatically counted. The
698 spontaneous rotation test lasted 5 min. Apomorphine-evoked rotational asymmetry was
699 evaluated for 60 min after s.c. administration of apomorphine hydrochloride (0.25 mg/kg)
700 dissolved in physiological saline containing 0.1% ascorbic acid (Sigma Aldrich, St. Louis,
701 Missouri, USA). Two priming injections of apomorphine (1-week interval off-drug) were necessary
702 to produce sensitization to the treatment. The program RotaMeter (TSE Systems GmbH, Bad
703 Homburg, Germany) was used to acquire the data. Data were analyzed as follows:

$$\text{turns/min} = \text{ccw rotation} - \text{cw rotations}$$

704

705 *Beam walk test*

706 Rats were trained for 4 days to cross a built-in-house beam (1.7 cm width, 60 cm length, 40 cm
707 height), and reach a cage with environmental enrichment. Rats had 5 trials to cross the beam
708 with the reward resting time decreasing from 30 s to 10 s. On the test day (one week apart from
709 the fourth day of training), rats were videotaped. The acquired videos were analyzed using a

710 slow-motion video player (VLC software, VideoLan) and the number of footslips (falls) was
711 counted. Data were analyzed as follows:

$$\text{contralateral footslips (\% to total steps)} = \frac{\text{contralateral footslips}}{\text{total steps}} \times 100$$

712
713 *Open Field test*
714 Untrained rats were set in a rectangular box (TSE Systems GmbH, Bad Homburg, Germany) for
715 11 min (1 min habituation, 10 min test) to evaluate the spontaneous exploratory behavior. A
716 frame with light sensors, as high as the animals' body center, was connected to a receiver box to
717 record the rats' walked distance. The program ActiMod (TSE Systems GmbH, Bad Homburg,
718 Germany) was used for the analysis and the experimental session was divided into 1 min time
719 bins. Results were averaged from the total traveled distance over 10 min (mean \pm SD).

720
721 *Body weight gain*
722 Rats' body weight was measured before (week 0) and 14 weeks after CRISPR/SaCas9-induced
723 VMAT2 knockdown. Body weight gain was calculated as follows:

$$\text{body weight gain (g)} = \frac{\text{weight at week 14} - \text{weight at week 0}}{\text{weight at week 0}} \times 100$$

724
725 **Histology of rat brain slices**
726 Rats of cohort 1 (n= 20) were sacrificed 19 weeks after viral vector injection via CO₂ inhalation
727 followed by intracardial perfusion with heparinized DPBS (1:50 v/v, 100 mL). After decapitation,
728 brains were rapidly removed and placed in a brain matrix on ice. The left and right striata were
729 dissected, from 2 mm thick coronal sections, flash-frozen in liquid nitrogen, and stored at – 80 °C
730 until further analysis (HPLC). The remaining tissue was fixed in 4% paraformaldehyde for 48 h

731 and then transferred to a 20% sucrose solution for cryoprotection. Brains were cut into 35 µm
732 thick coronal sections on a freezing microtome (Leica Biosystems, Wetzlar, Germany) and stored
733 in an anti-freeze solution (0.5 M phosphate buffer, 30 % glycerol, 30 % ethylene glycol) at -
734 20 °C. Sections were collected in 12 equally spaced series through the entire anterior-posterior
735 extent of the SN and striatum and stored until further analysis. Immunohistochemistry was
736 performed on free-floating sections. Sections were washed 3 times with TBS buffer and antigen
737 retrieval was carried for 30 min at 80 °C in Tris/EDTA buffer. Afterward, pre-incubation in MeOH
738 (10%) and H₂O₂ (3%) in TBS was performed for 30 min. Following the blocking in 5% normal
739 goat serum in TBS-X (0.05%), primary antibody incubation was performed for 24 h at room
740 temperature in 1% BSA in TBS-X (TH: 1:5000, P40101, Pel-freez, Arkansas, USA, VMAT2:
741 1:5000, 20042, Immunostar, Hudson, USA). The tissue was rinsed in TBS-X and reacted with the
742 respective biotinylated secondary antibody (1:200, Vector Laboratories Ltd., Peterborough, UK)
743 for 60 min at room temperature in 1% BSA in TBS-X. Staining was developed using 3,3'-
744 diaminobenzidine (DAB Substrate Kit, Vector Laboratories Ltd., Peterborough, UK) and an
745 immunoperoxidase system (Vectastain Elite ABC-Kit, Vector Laboratories Ltd., Peterborough,
746 UK). Slices were rinsed, mounted onto chromalum gelatinized slides, dehydrated in ascending
747 concentrations of alcohol and xylene baths, and coverslipped with DPX mounting medium (Sigma
748 Aldrich, St. Louis, Missouri, USA).

749

750 **Stereological analysis**

751 Estimates of total numbers of TH+ cells in nigral sections were obtained with an unbiased
752 stereological quantification method by employing the optical fractionator principle [120]. Brain
753 sections from 5 rats (VMAT2 knockdown n= 2, Control n= 3) were excluded from the stereological
754 analysis, due to weak TH immunoreactivity. First, 5x images were acquired with the automated
755 Metafer slide scanning platform (MetaSystems, Altlußheim, Germany). Then, ROIs were drawn
756 using the VSViewer program (Metasystems, Altlußheim, Germany), and a sampling fraction of

757 50% was defined. Afterward, 63x images were acquired in an automated fashion based on the
758 sampling fraction in a random orientation within the ROI. The acquired 63x images were imported
759 into the VIS program and cell counting was performed with the CAST module (Visiopharm A/S,
760 Hørsholm, Denmark, Version 2020.08.2.8800).

761 The number of cells estimates was obtained by applying the formula:

$$Total\ number\ of\ TH +\ cells = \sum \left(\frac{Number\ of\ cells\ counted\ per\ brain}{Acquisition\ fraction\ x\ counting\ frame} \right) \times number\ of\ series$$

762

763 **Immunofluorescence of rat brain slices**

764 Immunofluorescence was performed on SN sections from rats of cohort 1 (35 µm thick coronal
765 sections), mounted onto chromalum gelatinized slides, dehydrated in ascending concentrations of
766 alcohol and xylene baths. Sections were washed 3 times with KPBS buffer and antigen retrieval
767 was carried for 30 min at 80 °C in Tris/EDTA buffer. Following blocking in 5% donkey serum and
768 normal horse serum in KPBS-X (0.25%), primary antibody incubation was performed for 24 h at
769 room temperature (VMAT2: 1:5000, 20042, Immunostar, Hudson, USA, HA-tag: 1:5000, MMS-
770 101R, Nordic BioSite, Taby, Sweden, GFP: 1:50.000, ab13970, Abcam, Cambridge, UK). The
771 tissue was rinsed in KPBS-X and reacted with the respective fluorophore-conjugated secondary
772 antibody (1:200, Vector Laboratories Ltd., Peterborough, UK) for 2 h in 0.2% KPBS-X. Slides
773 were coverslipped with Vectashield mounting medium (Vector Laboratories Ltd., Peterborough,
774 UK).

775

776 **Biochemistry**

777 Dopamine, 3,4-Dihydroxyphenylacetic acid (DOPAC), homovanillic acid (HVA), and serotonin (5-
778 HT) striatal levels were determined by HPLC. Brain samples from 5 rats (VMAT2 knockdown

779 n= 3, Control n= 2) were excluded from the analysis as striatal sections did not fall in the selected
780 range: 1.2 – 0.4 mm.

781 Briefly, striatal brain lysates generated from cohort 1 were injected by a cooled autosampler into
782 an ESA Coulchem III coupled to a Decade Elite electrochemical detector (Antec Scientific,
783 Zoeterwoude, The Netherlands) set to a potential of +350 mV. Separation was facilitated by using
784 an Atlantis Premier BEH C18 AX column (Waters Corporation, Massachusetts, USA) and a dual
785 mobile phase gradient of decreasing octane sulfonic acid (OSA) and increasing MeOH content
786 (mobile phase A containing 100 mM PO₄-buffer pH 2.50 and 4.62 mM OSA and mobile phase B
787 containing 100 mM PO₄-buffer pH 2.50 and 2.31 mM OSA), delivered at a flow rate of
788 0.35 mL/min to an Atlantis Premier BEH C18 column (particle size 2.5 µm, 2.1 mm x 150 mm)
789 (Waters Corporation, Massachusetts, USA). Data was collected using the Chemstation software
790 (Agilent, California, USA) and then exported to Chromeleon (LifeTechnologies, Massachusetts,
791 USA) for data quality control, peak integration, and concentration calculations. Striatal
792 metabolites' content was expressed in nmol for each sample and normalized to total protein (mg).
793 Dopamine turnover rate was calculated according to the formula:

$$\text{Dopamine turnover rate} = \frac{HVA + DOPAC}{DA}$$

794

795 **Statistics**

796 Statistical analysis was performed with GraphPad Prism 9.0 (Graphpad Software) if not otherwise
797 stated. Results were analyzed using paired t-tests for the within-subjects comparisons, and
798 unpaired t-tests for the between-groups comparisons. Correlations were performed using linear
799 regression analyses. Synaptic dysfunction discrimination was tested with multiple-comparison
800 ANOVA.

801

802 Bibliography

803 1. Biswal, B., et al., *Functional connectivity in the motor cortex of resting human brain using echo-*
804 *planar MRI*. *Magn Reson Med*, 1995. **34**(4): p. 537-41.

805 2. Ogawa, S., et al., *Brain magnetic resonance imaging with contrast dependent on blood*
806 *oxygenation*. *Proc Natl Acad Sci U S A*, 1990. **87**(24): p. 9868-72.

807 3. Lu, H., et al., *Rat brains also have a default mode network*. *Proc Natl Acad Sci U S A*, 2012.
808 **109**(10): p. 3979-84.

809 4. Becerra, L., et al., *Robust reproducible resting state networks in the awake rodent brain*. *PLoS*
810 *One*, 2011. **6**(10): p. e25701.

811 5. Fox, M.D., et al., *The human brain is intrinsically organized into dynamic, anticorrelated functional*
812 *networks*. *Proc Natl Acad Sci U S A*, 2005. **102**(27): p. 9673-8.

813 6. Jonckers, E., et al., *Functional connectivity fMRI of the rodent brain: comparison of functional*
814 *connectivity networks in rat and mouse*. *PLoS One*, 2011. **6**(4): p. e18876.

815 7. Wehrl, H.F., et al., *Simultaneous PET-MRI reveals brain function in activated and resting state on*
816 *metabolic, hemodynamic and multiple temporal scales*. *Nat Med*, 2013. **19**(9): p. 1184-9.

817 8. Amend, M., et al., *Functional resting-state brain connectivity is accompanied by dynamic*
818 *correlations of application-dependent [(18)F]FDG PET-tracer fluctuations*. *Neuroimage*, 2019. **196**:
819 p. 161-172.

820 9. Ionescu, T.M., et al., *Elucidating the complementarity of resting-state networks derived from*
821 *dynamic [(18)F]FDG and hemodynamic fluctuations using simultaneous small-animal PET/MRI*.
822 *Neuroimage*, 2021. **236**: p. 118045.

823 10. Badhwar, A., et al., *Resting-state network dysfunction in Alzheimer's disease: A systematic review*
824 *and meta-analysis*. *Alzheimers Dement (Amst)*, 2017. **8**: p. 73-85.

825 11. Bluhm, R.L., et al., *Spontaneous low-frequency fluctuations in the BOLD signal in schizophrenic*
826 *patients: anomalies in the default network*. *Schizophr Bull*, 2007. **33**(4): p. 1004-12.

827 12. Volkow, N.D., et al., *Imaging endogenous dopamine competition with [11C]raclopride in the*
828 *human brain*. *Synapse*, 1994. **16**(4): p. 255-62.

829 13. Laruelle, M., *Imaging synaptic neurotransmission with in vivo binding competition techniques: a*
830 *critical review*. *J Cereb Blood Flow Metab*, 2000. **20**(3): p. 423-51.

831 14. Patel, V.D., et al., *Imaging dopamine release with Positron Emission Tomography (PET) and (11)C-*
832 *raclopride in freely moving animals*. *Neuroimage*, 2008. **41**(3): p. 1051-66.

833 15. Roffman, J.L., et al., *Dopamine D1 signaling organizes network dynamics underlying working*
834 *memory*. *Science advances*, 2016. **2**(6): p. e1501672-e1501672.

835 16. McCutcheon, R.A., et al., *Mesolimbic Dopamine Function Is Related to Salience Network*
836 *Connectivity: An Integrative Positron Emission Tomography and Magnetic Resonance Study*. *Biol*
837 *Psychiatry*, 2019. **85**(5): p. 368-378.

838 17. Nagano-Saito, A., et al., *Posterior dopamine D2/3 receptors and brain network functional*
839 *connectivity*. *Synapse*, 2017. **71**(11).

840 18. Hahn, A., et al., *Differential modulation of the default mode network via serotonin-1A receptors*.
841 *Proc Natl Acad Sci U S A*, 2012. **109**(7): p. 2619-24.

842 19. Vidal, B., et al., *In vivo biased agonism at 5-HT(1A) receptors: characterisation by simultaneous*
843 *PET/MR imaging*. *Neuropsychopharmacology*, 2018. **43**(11): p. 2310-2319.

844 20. Shiyam Sundar, L.K., et al., *Fully Integrated PET/MR Imaging for the Assessment of the*
845 *Relationship Between Functional Connectivity and Glucose Metabolic Rate*. *Front Neurosci*, 2020.
846 **14**: p. 252.

847 21. Sander, C.Y., et al., *Imaging Agonist-Induced D2/D3 Receptor Desensitization and Internalization*
848 *In Vivo with PET/fMRI*. *Neuropsychopharmacology*, 2016. **41**(5): p. 1427-36.

849 22. Ionescu, T.M., et al., *Striatal and prefrontal D2R and SERT distributions contrastingly correlate*
850 *with default-mode connectivity*. *Neuroimage*, 2021. **243**: p. 118501.

851 23. Betley, J.N. and S.M. Sternson, *Adeno-associated viral vectors for mapping, monitoring, and*
852 *manipulating neural circuits*. *Hum Gene Ther*, 2011. **22**(6): p. 669-77.

853 24. Jinek, M., et al., *RNA-programmed genome editing in human cells*. *Elife*, 2013. **2**: p. e00471.

854 25. Cong, L., et al., *Multiplex genome engineering using CRISPR/Cas systems*. *Science*, 2013.
855 **339**(6121): p. 819-23.

856 26. Whitworth, K.M., et al., *Use of the CRISPR/Cas9 system to produce genetically engineered pigs*
857 *from in vitro-derived oocytes and embryos*. *Biol Reprod*, 2014. **91**(3): p. 78.

858 27. Chen, Y., et al., *Functional disruption of the dystrophin gene in rhesus monkey using CRISPR/Cas9*.
859 *Hum Mol Genet*, 2015. **24**(13): p. 3764-74.

860 28. Chang, N., et al., *Genome editing with RNA-guided Cas9 nuclease in zebrafish embryos*. *Cell Res*,
861 2013. **23**(4): p. 465-72.

862 29. Platt, R.J., et al., *CRISPR-Cas9 knockin mice for genome editing and cancer modeling*. *Cell*, 2014.
863 **159**(2): p. 440-55.

864 30. Yu, Z., et al., *Highly efficient genome modifications mediated by CRISPR/Cas9 in Drosophila*.
865 *Genetics*, 2013. **195**(1): p. 289-91.

866 31. Musunuru, K., et al., *In vivo CRISPR base editing of PCSK9 durably lowers cholesterol in primates*.
867 *Nature*, 2021. **593**(7859): p. 429-434.

868 32. Ousterout, D.G., et al., *Multiplex CRISPR/Cas9-based genome editing for correction of dystrophin*
869 *mutations that cause Duchenne muscular dystrophy*. *Nat Commun*, 2015. **6**: p. 6244.

870 33. Swiech, L., et al., *In vivo interrogation of gene function in the mammalian brain using CRISPR-
871 Cas9*. *Nature Biotechnology*, 2015. **33**(1): p. 102-U286.

872 34. Wilbie, D., J. Walther, and E. Mastrobattista, *Delivery Aspects of CRISPR/Cas for in Vivo Genome
873 Editing*. *Accounts of chemical research*, 2019. **52**(6): p. 1555-1564.

874 35. Wu, W.Y., et al., *Genome editing by natural and engineered CRISPR-associated nucleases*. *Nat
875 Chem Biol*, 2018. **14**(7): p. 642-651.

876 36. Zetsche, B., et al., *Cpf1 is a single RNA-guided endonuclease of a class 2 CRISPR-Cas system*. *Cell*,
877 2015. **163**(3): p. 759-71.

878 37. Kleinstiver, B.P., et al., *Engineered CRISPR-Cas9 nucleases with altered PAM specificities*. *Nature*,
879 2015. **523**(7561): p. 481-5.

880 38. Ran, F.A., et al., *In vivo genome editing using *Staphylococcus aureus* Cas9*. *Nature*, 2015.
881 **520**(7546): p. 186-91.

882 39. Nishimasu, H., et al., *Crystal Structure of *Staphylococcus aureus* Cas9*. *Cell*, 2015. **162**(5): p. 1113-
883 26.

884 40. Sun, H., et al., *Development of a CRISPR-SaCas9 system for projection- and function-specific gene
885 editing in the rat brain*. *Sci Adv*, 2020. **6**(12): p. eaay6687.

886 41. Kumar, N., et al., *The Development of an AAV-Based CRISPR SaCas9 Genome Editing System That
887 Can Be Delivered to Neurons in vivo and Regulated via Doxycycline and Cre-Recombinase*. *Front
888 Mol Neurosci*, 2018. **11**: p. 413.

889 42. Hunker, A.C., et al., *Conditional Single Vector CRISPR/SaCas9 Viruses for Efficient Mutagenesis in
890 the Adult Mouse Nervous System*. *Cell Rep*, 2020. **30**(12): p. 4303-4316 e6.

891 43. Liu, Y. and R.H. Edwards, *The role of vesicular transport proteins in synaptic transmission and
892 neural degeneration*. *Annu Rev Neurosci*, 1997. **20**: p. 125-56.

893 44. Miyanishi, K., et al., *Behavioral tests predicting striatal dopamine level in a rat hemi-Parkinson's
894 disease model*. *Neurochem Int*, 2019. **122**: p. 38-46.

895 45. Tomasi, D., et al., *Dopamine transporters in striatum correlate with deactivation in the default
896 mode network during visuospatial attention*. *PLoS One*, 2009. **4**(6): p. e6102.

897 46. Sambataro, F., et al., *DRD2 genotype-based variation of default mode network activity and of its*
898 *relationship with striatal DAT binding.* Schizophr Bull, 2013. **39**(1): p. 206-16.

899 47. Tritsch, N.X., J.B. Ding, and B.L. Sabatini, *Dopaminergic neurons inhibit striatal output through*
900 *non-canonical release of GABA.* Nature, 2012. **490**(7419): p. 262-6.

901 48. Tritsch, N.X., et al., *Midbrain dopamine neurons sustain inhibitory transmission using plasma*
902 *membrane uptake of GABA, not synthesis.* Elife, 2014. **3**: p. e01936.

903 49. Chatterjee, D., et al., *Enhanced CNS transduction from AAV.PHP.eB infusion into the cisterna*
904 *magna of older adult rats compared to AAV9.* Gene Ther, 2021.

905 50. Hume, S.P., et al., *Effect of L-dopa and 6-hydroxydopamine lesioning on [11C]raclopride binding in*
906 *rat striatum, quantified using PET.* Synapse, 1995. **21**(1): p. 45-53.

907 51. Mishra, R.K., A.M. Marshall, and S.L. Varmuza, *Supersensitivity in rat caudate nucleus: effects of 6-*
908 *hydroxydopamine on the time course of dopamine receptor and cyclic AMP changes.* Brain Res,
909 1980. **200**(1): p. 47-57.

910 52. Creese, I., D.R. Burt, and S.H. Snyder, *Dopamine receptor binding enhancement accompanies*
911 *lesion-induced behavioral supersensitivity.* Science, 1977. **197**(4303): p. 596-8.

912 53. Konieczny, J., et al., *The significance of rotational behavior and sensitivity of striatal dopamine*
913 *receptors in hemiparkinsonian rats: A comparative study of lactacystin and 6-OHDA.*
914 *Neuroscience*, 2017. **340**: p. 308-318.

915 54. Wang, Y.M., et al., *Knockout of the vesicular monoamine transporter 2 gene results in neonatal*
916 *death and supersensitivity to cocaine and amphetamine.* Neuron, 1997. **19**(6): p. 1285-96.

917 55. Seeman, P., et al., *Dopamine receptors in the central nervous system.* Fed Proc, 1978. **37**(2): p.
918 131-6.

919 56. Gnanalingham, K.K. and R.G. Robertson, *The effects of chronic continuous versus intermittent*
920 *levodopa treatments on striatal and extrastriatal D1 and D2 dopamine receptors and dopamine*
921 *uptake sites in the 6-hydroxydopamine lesioned rat--an autoradiographic study.* Brain Res, 1994.
922 **640**(1-2): p. 185-94.

923 57. Graham, W.C., A.R. Crossman, and G.N. Woodruff, *Autoradiographic studies in animal models of*
924 *hemi-parkinsonism reveal dopamine D2 but not D1 receptor supersensitivity. I. 6-OHDA lesions of*
925 *ascending mesencephalic dopaminergic pathways in the rat.* Brain Res, 1990. **514**(1): p. 93-102.

926 58. Antonini, A., et al., *Long-term changes of striatal dopamine D2 receptors in patients with*
927 *Parkinson's disease: a study with positron emission tomography and [11C]raclopride.* Mov Disord,
928 1997. **12**(1): p. 33-8.

929 59. Kraemer, J., et al., *Correlation of striatal dopamine transporter imaging with post mortem*
930 *substantia nigra cell counts.* Mov Disord, 2014. **29**(14): p. 1767-73.

931 60. Sossi, V., et al., *Dopamine transporter relation to levodopa-derived synaptic dopamine in a rat*
932 *model of Parkinson's: an in vivo imaging study.* J Neurochem, 2009. **109**(1): p. 85-92.

933 61. Zigmund, M.J., T.G. Hastings, and R.G. Perez, *Increased dopamine turnover after partial loss of*
934 *dopaminergic neurons: compensation or toxicity?* Parkinsonism Relat Disord, 2002. **8**(6): p. 389-
935 93.

936 62. Takahashi, N., et al., *VMAT2 knockout mice: heterozygotes display reduced amphetamine-*
937 *conditioned reward, enhanced amphetamine locomotion, and enhanced MPTP toxicity.* Proc Natl
938 Acad Sci U S A, 1997. **94**(18): p. 9938-43.

939 63. Fon, E.A., et al., *Vesicular transport regulates monoamine storage and release but is not essential*
940 *for amphetamine action.* Neuron, 1997. **19**(6): p. 1271-83.

941 64. Mooslehner, K.A., et al., *Mice with very low expression of the vesicular monoamine transporter 2*
942 *gene survive into adulthood: potential mouse model for parkinsonism.* Mol Cell Biol, 2001. **21**(16):
943 p. 5321-31.

944 65. Caudle, W.M., et al., *Reduced vesicular storage of dopamine causes progressive nigrostriatal*
945 *neurodegeneration.* J Neurosci, 2007. **27**(30): p. 8138-48.

946 66. Taylor, T.N., et al., *Nonmotor symptoms of Parkinson's disease revealed in an animal model with*
947 *reduced monoamine storage capacity.* J Neurosci, 2009. **29**(25): p. 8103-13.

948 67. Back, S., et al., *Neuron-Specific Genome Modification in the Adult Rat Brain Using CRISPR-Cas9*
949 *Transgenic Rats.* Neuron, 2019.

950 68. Zimmer, E.R., et al., *MicroPET imaging and transgenic models: a blueprint for Alzheimer's disease*
951 *clinical research.* Trends Neurosci, 2014. **37**(11): p. 629-41.

952 69. Andrews-Hanna, J.R., *The brain's default network and its adaptive role in internal mentation.*
953 Neuroscientist, 2012. **18**(3): p. 251-70.

954 70. Gottlich, M., et al., *Altered resting state brain networks in Parkinson's disease.* PLoS One, 2013.
955 **8**(10): p. e77336.

956 71. Huang, S., et al., *Multisensory Competition Is Modulated by Sensory Pathway Interactions with*
957 *Fronto-Sensorimotor and Default-Mode Network Regions.* J Neurosci, 2015. **35**(24): p. 9064-77.

958 72. Wu, C.W., et al., *Synchrony Between Default-Mode and Sensorimotor Networks Facilitates Motor*
959 *Function in Stroke Rehabilitation: A Pilot fMRI Study.* Front Neurosci, 2020. **14**: p. 548.

960 73. Wang, J., et al., *Functional reorganization of intra- and internetwork connectivity in major*
961 *depressive disorder after electroconvulsive therapy.* Hum Brain Mapp, 2018. **39**(3): p. 1403-1411.

962 74. Perlberg, V., et al., *Alterations of the nigrostriatal pathway in a 6-OHDA rat model of Parkinson's*
963 *disease evaluated with multimodal MRI.* PLoS One, 2018. **13**(9): p. e0202597.

964 75. Monnot, C., et al., *Asymmetric dopaminergic degeneration and levodopa alter functional*
965 *corticostriatal connectivity bilaterally in experimental parkinsonism.* Exp Neurol, 2017. **292**: p. 11-
966 20.

967 76. Honey, G.D., et al., *Dopaminergic drug effects on physiological connectivity in a human cortico-*
968 *striato-thalamic system.* Brain, 2003. **126**(Pt 8): p. 1767-81.

969 77. Kwak, Y., et al., *Altered resting state cortico-striatal connectivity in mild to moderate stage*
970 *Parkinson's disease.* Front Syst Neurosci, 2010. **4**: p. 143.

971 78. Costa, R.M., et al., *Rapid alterations in cortico-striatal ensemble coordination during acute*
972 *dopamine-dependent motor dysfunction.* Neuron, 2006. **52**(2): p. 359-69.

973 79. Gatev, P., O. Darbin, and T. Wichmann, *Oscillations in the basal ganglia under normal conditions*
974 *and in movement disorders.* Mov Disord, 2006. **21**(10): p. 1566-77.

975 80. Hammond, C., H. Bergman, and P. Brown, *Pathological synchronization in Parkinson's disease:*
976 *networks, models and treatments.* Trends Neurosci, 2007. **30**(7): p. 357-64.

977 81. Eusebio, A., et al., *Resonance in subthalamo-cortical circuits in Parkinson's disease.* Brain, 2009.
978 **132**(Pt 8): p. 2139-50.

979 82. Brazhnik, E., et al., *State-dependent spike and local field synchronization between motor cortex*
980 *and substantia nigra in hemiparkinsonian rats.* J Neurosci, 2012. **32**(23): p. 7869-80.

981 83. Moran, R.J., et al., *Alterations in brain connectivity underlying beta oscillations in Parkinsonism.*
982 PLoS Comput Biol, 2011. **7**(8): p. e1002124.

983 84. Gerfen, C.R. and D.J. Surmeier, *Modulation of striatal projection systems by dopamine.* Annu Rev
984 Neurosci, 2011. **34**: p. 441-66.

985 85. Caspers, J., et al., *Differential Functional Connectivity Alterations of Two Subdivisions within the*
986 *Right dlPFC in Parkinson's Disease.* Front Hum Neurosci, 2017. **11**: p. 288.

987 86. Owens-Walton, C., et al., *Increased functional connectivity of thalamic subdivisions in patients*
988 *with Parkinson's disease.* PLoS One, 2019. **14**(9): p. e0222002.

989 87. Kahn, I., et al., *Distinct cortical anatomy linked to subregions of the medial temporal lobe revealed*
990 *by intrinsic functional connectivity.* J Neurophysiol, 2008. **100**(1): p. 129-39.

991 88. Vincent, J.L., et al., *Coherent spontaneous activity identifies a hippocampal-parietal memory*
992 *network.* J Neurophysiol, 2006. **96**(6): p. 3517-31.

993 89. Hillary, F.G., et al., *Hyperconnectivity is a fundamental response to neurological disruption.*
994 Neuropsychology, 2015. **29**(1): p. 59-75.

995 90. Klobusiakova, P., et al., *Connectivity Between Brain Networks Dynamically Reflects Cognitive*
996 *Status of Parkinson's Disease: A Longitudinal Study.* J Alzheimers Dis, 2019. **67**(3): p. 971-984.

997 91. Mevel, K., et al., *The default mode network in healthy aging and Alzheimer's disease.* Int J
998 Alzheimers Dis, 2011. **2011**: p. 535816.

999 92. Gorges, M., et al., *To rise and to fall: functional connectivity in cognitively normal and cognitively*
1000 *impaired patients with Parkinson's disease.* Neurobiol Aging, 2015. **36**(4): p. 1727-1735.

1001 93. Helmich, R.C., et al., *Spatial remapping of cortico-striatal connectivity in Parkinson's disease.*
1002 Cereb Cortex, 2010. **20**(5): p. 1175-86.

1003 94. O'Gorman Tuura, R.L., C.R. Baumann, and H. Baumann-Vogel, *Beyond Dopamine: GABA,*
1004 *Glutamate, and the Axial Symptoms of Parkinson Disease.* Front Neurol, 2018. **9**: p. 806.

1005 95. Whiting, P.J., *The GABAA receptor gene family: new opportunities for drug development.* Curr
1006 Opin Drug Discov Devel, 2003. **6**(5): p. 648-57.

1007 96. Kapogiannis, D., et al., *Posteromedial cortex glutamate and GABA predict intrinsic functional*
1008 *connectivity of the default mode network.* Neuroimage, 2013. **64**: p. 112-9.

1009 97. Douaud, G., et al., *Integration of structural and functional magnetic resonance imaging in*
1010 *amyotrophic lateral sclerosis.* Brain, 2011. **134**(Pt 12): p. 3470-9.

1011 98. Levar, N., et al., *Anterior cingulate GABA and glutamate concentrations are associated with*
1012 *resting-state network connectivity.* Sci Rep, 2019. **9**(1): p. 2116.

1013 99. Lanoue, A.C., G.J. Blatt, and J.J. Soghomonian, *Decreased parvalbumin mRNA expression in*
1014 *dorsolateral prefrontal cortex in Parkinson's disease.* Brain Res, 2013. **1531**: p. 37-47.

1015 100. Lanoue, A.C., et al., *Decreased glutamic acid decarboxylase mRNA expression in prefrontal cortex*
1016 *in Parkinson's disease.* Exp Neurol, 2010. **226**(1): p. 207-17.

1017 101. Ihara, M., et al., *Association of vascular parkinsonism with impaired neuronal integrity in the*
1018 *striatum.* J Neural Transm (Vienna), 2007. **114**(5): p. 577-84.

1019 102. van Nuland, A.J.M., et al., *GABAergic changes in the thalamocortical circuit in Parkinson's disease.*
1020 Hum Brain Mapp, 2020. **41**(4): p. 1017-1029.

1021 103. Allen, P., et al., *Extrinsic and default mode networks in psychiatric conditions: Relationship to*
1022 *excitatory-inhibitory transmitter balance and early trauma.* Neurosci Biobehav Rev, 2019. **99**: p.
1023 90-100.

1024 104. Liu, Z., et al., *Tissue Specific Expression of Cre in Rat Tyrosine Hydroxylase and Dopamine Active*
1025 *Transporter-Positive Neurons.* PLoS One, 2016. **11**(2): p. e0149379.

1026 105. Anders Björklund, S.B.D., *Dopamine neuron systems in the brain: an update.* Trends in
1027 Neuroscience, 2007. **30**(5): p. 194-202.

1028 106. Ran, F.A., et al., *Genome engineering using the CRISPR-Cas9 system.* Nat Protoc, 2013. **8**(11): p.
1029 2281-2308.

1030 107. Vouillot, L., A. Thelie, and N. Pollet, *Comparison of T7E1 and surveyor mismatch cleavage assays*
1031 *to detect mutations triggered by engineered nucleases.* G3 (Bethesda), 2015. **5**(3): p. 407-15.

1032 108. Huang, Z.R., et al., *A Novel Potential Positron Emission Tomography Imaging Agent for Vesicular*
1033 *Monoamine Transporter Type 2.* PLoS One, 2016. **11**(9): p. e0161295.

1034 109. Ding, Y.S., et al., *Pharmacokinetics and in vivo specificity of [11C]dl-threo-methylphenidate for the*
1035 *presynaptic dopaminergic neuron.* Synapse, 1994. **18**(2): p. 152-60.

1036 110. Wadsworth, H., et al., *[(1)(8)F]GE-180: a novel fluorine-18 labelled PET tracer for imaging*
1037 *Translocator protein 18 kDa (TSPO).* Bioorg Med Chem Lett, 2012. **22**(3): p. 1308-13.

1038 111. Paasonen, J., et al., *Functional connectivity under six anesthesia protocols and the awake*
1039 *condition in rat brain.* Neuroimage, 2018. **172**: p. 9-20.

1040 112. Lopez-Gonzalez, F.J., et al., *QModeling: a Multiplatform, Easy-to-Use and Open-Source Toolbox for*
1041 *PET Kinetic Analysis.* Neuroinformatics, 2019. **17**(1): p. 103-114.

1042 113. Schiffer, W.K., et al., *Serial microPET measures of the metabolic reaction to a microdialysis probe*
1043 *implant.* J Neurosci Methods, 2006. **155**(2): p. 272-84.

1044 114. Logan, J., *Graphical analysis of PET data applied to reversible and irreversible tracers*. Nucl Med
1045 Biol, 2000. **27**(7): p. 661-70.

1046 115. Judenhofer, M.S., et al., *Simultaneous PET-MRI: a new approach for functional and morphological*
1047 *imaging*. Nat Med, 2008. **14**(4): p. 459-65.

1048 116. Ionescu, T., *Striatal and prefrontal D2R and SERT distributions contrastingly correlate with default-*
1049 *mode connectivity*. 2021.

1050 117. Matthew Brett, J.-L.A., Romain Valabregue, Jean-Baptiste Poline, *Region of interest analysis using*
1051 *an SPM toolbox*, in *8th International Conference on Functional Mapping of the Human Brain*. June 2-
1052 6, 2002: Sendai, Japan.

1053 118. Rubinov, M. and O. Sporns, *Complex network measures of brain connectivity: uses and*
1054 *interpretations*. Neuroimage, 2010. **52**(3): p. 1059-69.

1055 119. Ungerstedt, U. and G.W. Arbuthnott, *Quantitative recording of rotational behavior in rats after 6-*
1056 *hydroxy-dopamine lesions of the nigrostriatal dopamine system*. Brain Res, 1970. **24**(3): p. 485-93.

1057 120. West, M.J., *Stereological methods for estimating the total number of neurons and synapses: issues*
1058 *of precision and bias*. Trends Neurosci, 1999. **22**(2): p. 51-61.

1059

1060

1061 **Acknowledgments**

1062 We are very grateful to Feng Zhang and all members of the laboratory, Broad Institute of MIT and
1063 Harvard, for the help and support with establishing the CRISPR gene knockdown experiments.
1064 We thank the technical assistants Sandro Aidone, Daniel Bukala, Linda Schramm, Maren Harant,
1065 Ramona Stremme, Elena Kimmerle and Johannes Kinzler. We also thank Ulla Samuelsson,
1066 Ulrika Sparrhult-Björk, Dr. Ulrika Schagerlöf, Anneli Josefsson and Anna Hansen at Lund
1067 University, Sweden for their technical support. Additionally, we acknowledge Dr. Julia Mannheim,
1068 Dr. Andreas Schmid, Dr. Rebecca Rock, Ines Herbon, Dr. Neele Hübner, Dr. Andreas Dieterich,
1069 Hans Jörg Rahm, Dr. Carsten Calaminus, Funda Cay, Kristin Patzwaldt, Laura Kübler, Marilena
1070 Poxleitner, Sabrina Buss and Dominik Seyfried for their administrative, technical, and
1071 experimental support at the Department of Preclinical Imaging and Radiopharmacy, Werner
1072 Siemens Imaging Center, Eberhard Karls University, Tuebingen. This study is also part of the
1073 PhD theses of Sabina Marciano and Tudor Mihai Ionescu.

1074 **Funding**

1075 • German Research Foundation to KH
1076 • Carl-Zeiss Foundation to KH
1077 • Werner Siemens Foundation to BJP
1078 • Deutscher Akademischer Austauschdienst to SM, KH

1079 **Author contributions**

1080 • Conceptualization: KH
1081 • Methodology: SM, TMI
1082 • Software: SM, TMI
1083 • Validation: SM
1084 • Formal analysis: SM, TMI

- 1085 • Investigation: SM, TMI, AM, RSS, RYC
- 1086 • Resources: BJP, DK
- 1087 • Data curation: SM
- 1088 • Writing – original draft: SM
- 1089 • Writing – review and editing: SM, TMI, AM, DK, RSS, RYC, BJP, KH
- 1090 • Supervision: KH
- 1091 • Project administration: KH
- 1092 • Funding acquisition: BJP, KH

1093 **Competing interests**

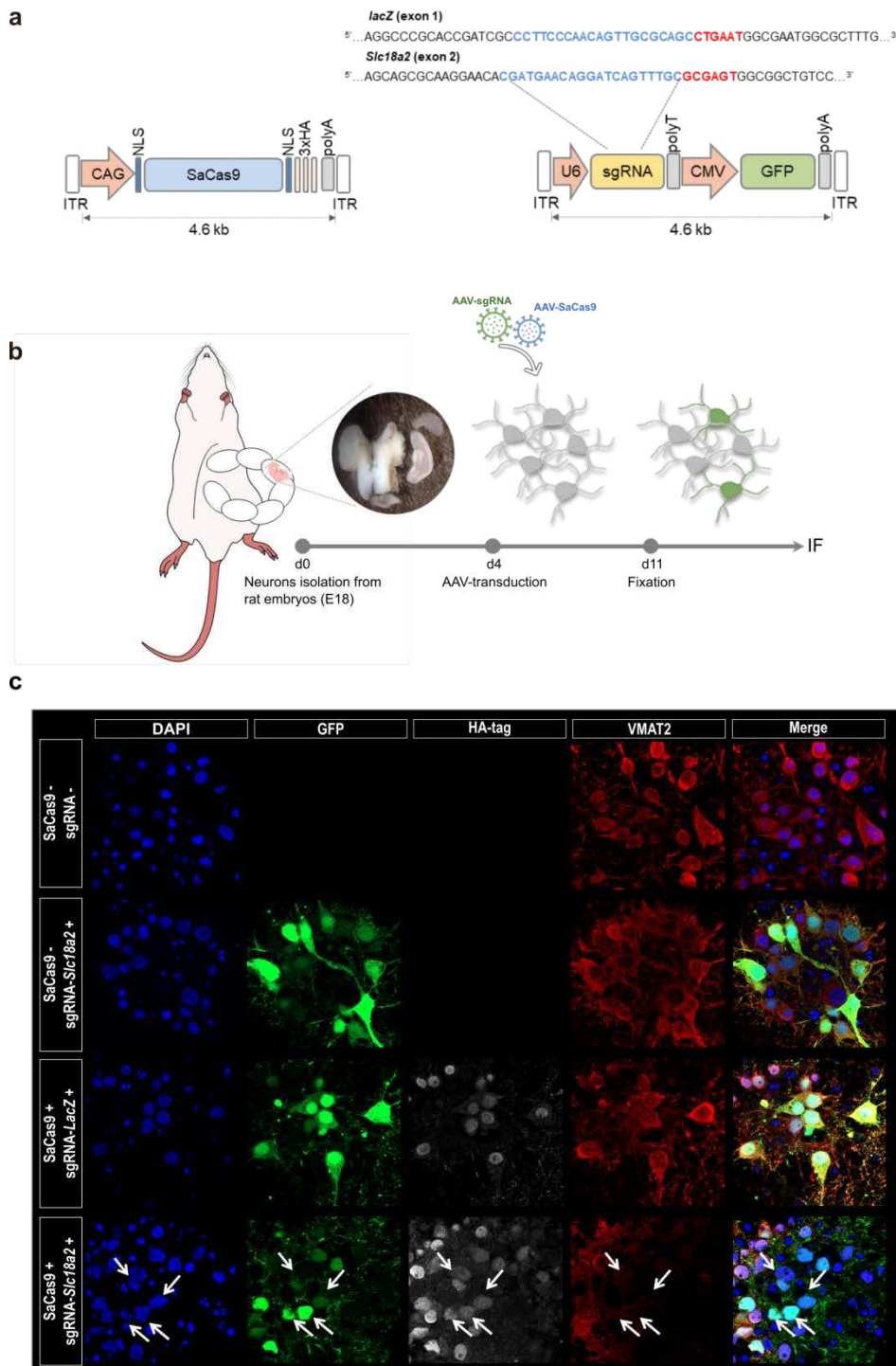
1094 The authors declare no conflict of interest.

1095 **Data availability**

1096 The original dataset will be made available upon request.

1097

1098 **Figures**



1099

1100

1101

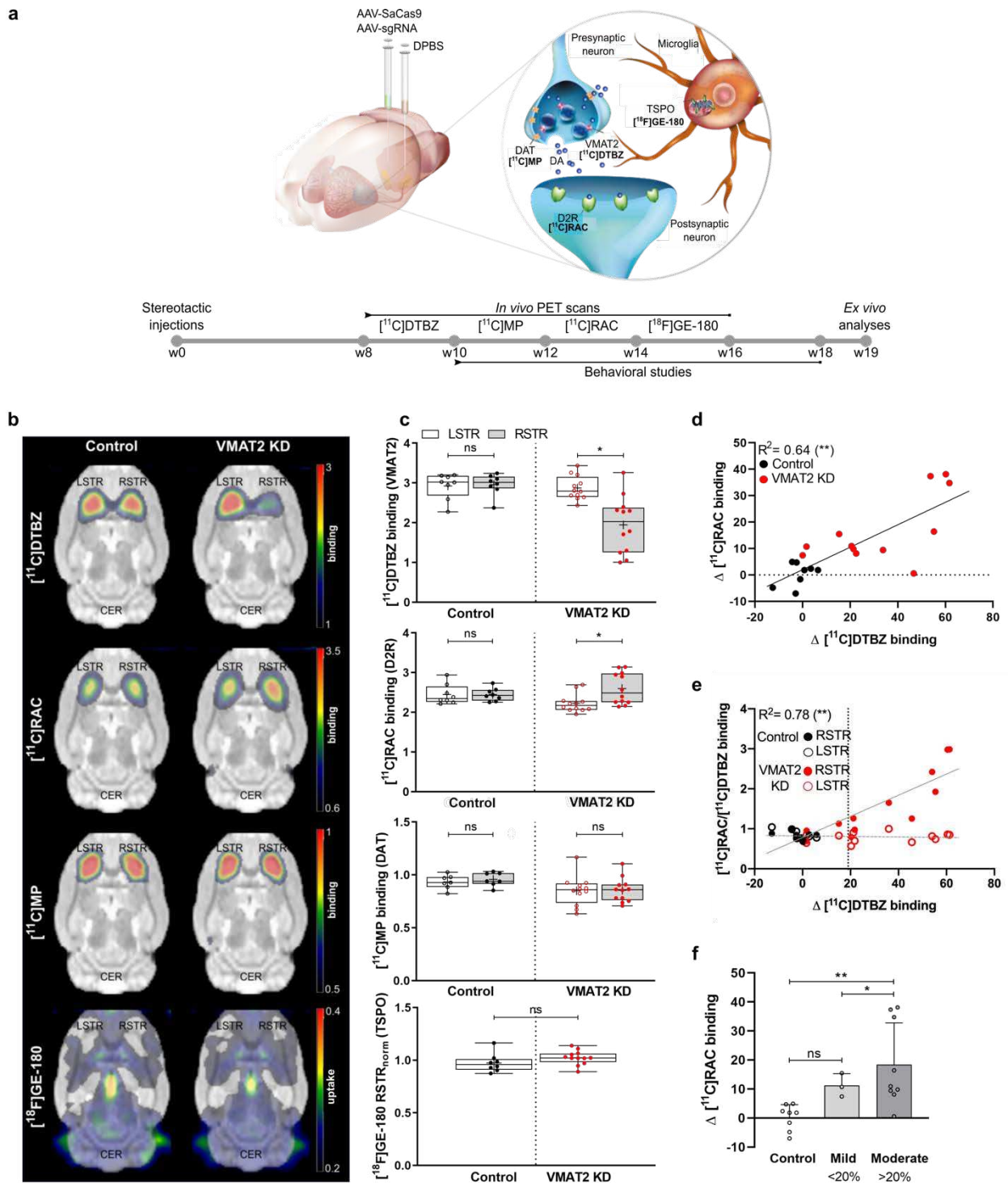
1102

1103

Fig. 1 *In vitro* validation of CRISPR/SaCas9-induced VMAT2 knockdown in rat primary cortical neurons. (a) AAV-SaCas9 and AAV-sgRNA expression vectors. (b) Experimental design for primary neurons isolation and transduction. (c) VMAT2 immunostaining (red), nuclei labeled with DAPI (blue). GFP (green) and HA-tag (white) indicate the expression of the sgRNA and SaCas9 vectors, respectively.

1104 VMAT2 KD (arrows) is shown in neurons transduced with AAVs carrying SaCas9 and sgRNA-*Slc18a2*. KD,
1105 knockdown; ITR, inverted terminal repeat; CMV, cytomegalovirus promoter; GFP, green fluorescent
1106 protein; CAG, CMV enhancer/chicken β-actin promoter; NLS, nuclear localization signal; HA-tag,
1107 hemagglutinin tag; polyA, polyadenylation signal; polyT, polytermination signal.

1108



1109

1110 **Fig. 2 CRISPR/SaCas9-induced VMAT2 knockdown elicits postsynaptic changes but no nerve**

1111 terminal loss or neuroinflammation in the adult rat brain. (a) Schematic illustration of the experimental

1112 design. (b) Mean binding potential and uptake maps of control and VMAT2 KD rats co-registered to a rat

1113 brain atlas. (c) Binding potential values of individual control and VMAT2 KD rats in the left and right

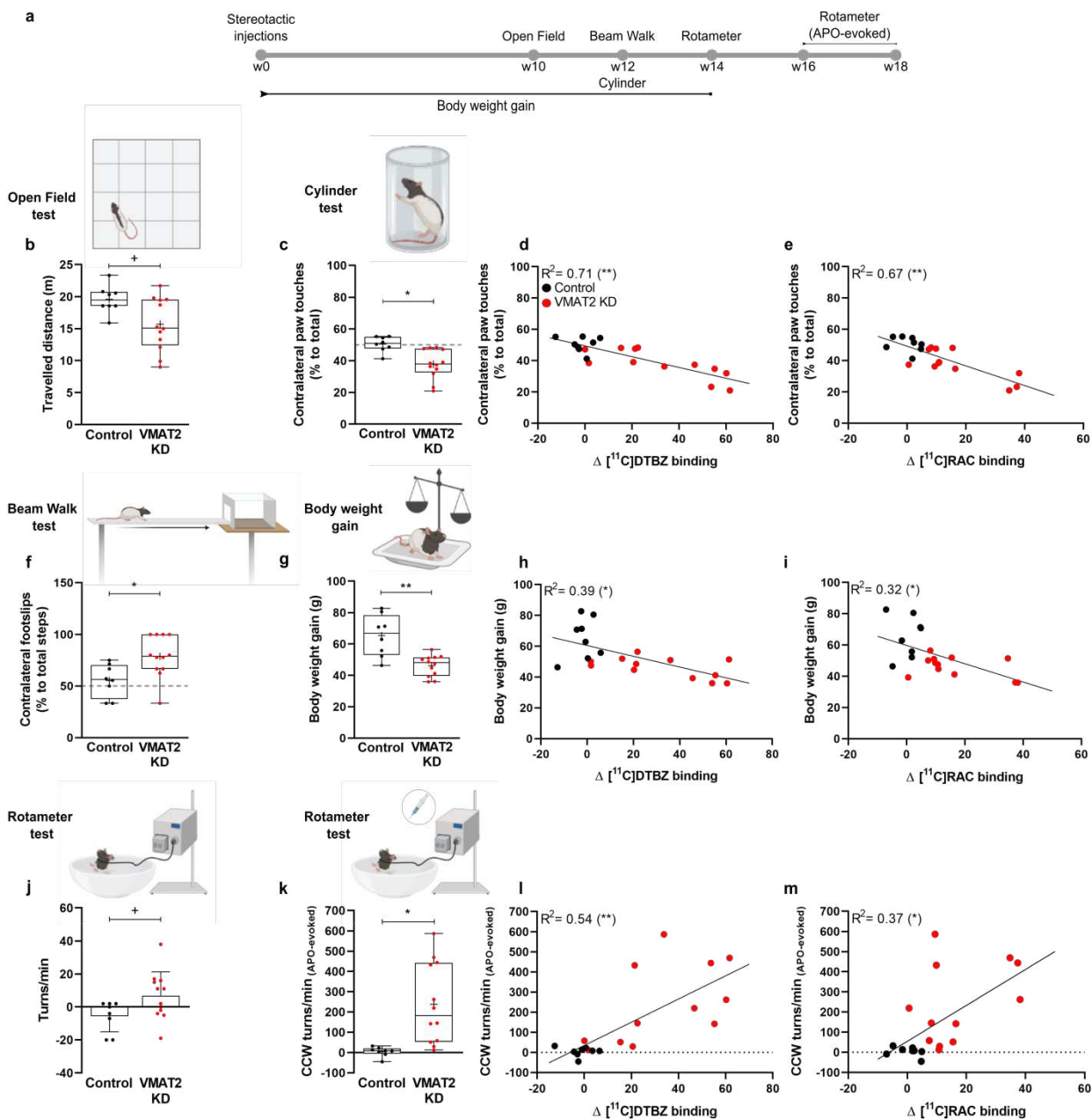
1114 striatum. For $[^{18}\text{F}]\text{GE}-180$ uptake values normalized to the left striatum are shown. (d) A strong correlation

1115 between $\Delta [^{11}\text{C}]\text{RAC}$ and $\Delta [^{11}\text{C}]\text{DTBZ}$ binding is shown. (e) Ratio of striatal $[^{11}\text{C}]\text{RAC}$ and $[^{11}\text{C}]\text{DTBZ}$

1116 binding shows prominent $[^{11}\text{C}]\text{RAC}$ changes when a threshold of $\sim 20\% \Delta [^{11}\text{C}]\text{DTBZ}$ binding is reached.

1117 This threshold was set to separate the VMAT2 KD rats into *mild* and *moderate*. (f) *Mild* and *moderate* rats
1118 could be differentiated based on the postsynaptic changes. * $P < 0.01$, ** $P < 0.001$, Bonferroni-Sidak
1119 corrected. Data are shown as boxplot with the median value (central mark), the mean value (plus sign),
1120 interquartile range (boxes edges), and the extreme points of the distribution (whiskers). Control rats n= 8;
1121 VMAT2 KD rats n= 12. *Mild*: Δ [¹¹C]DTBZ binding < 20%; *Moderate*: Δ [¹¹C]DTBZ binding \geq 20%. [¹¹C]MP,
1122 [¹¹C]methylphenidate; [¹¹C]RAC, [¹¹C]raclopride; LSTR, left striatum; RSTR, right striatum; CER,
1123 cerebellum; KD, knockdown; DAT, dopamine transporter; TSPO, translocator protein.

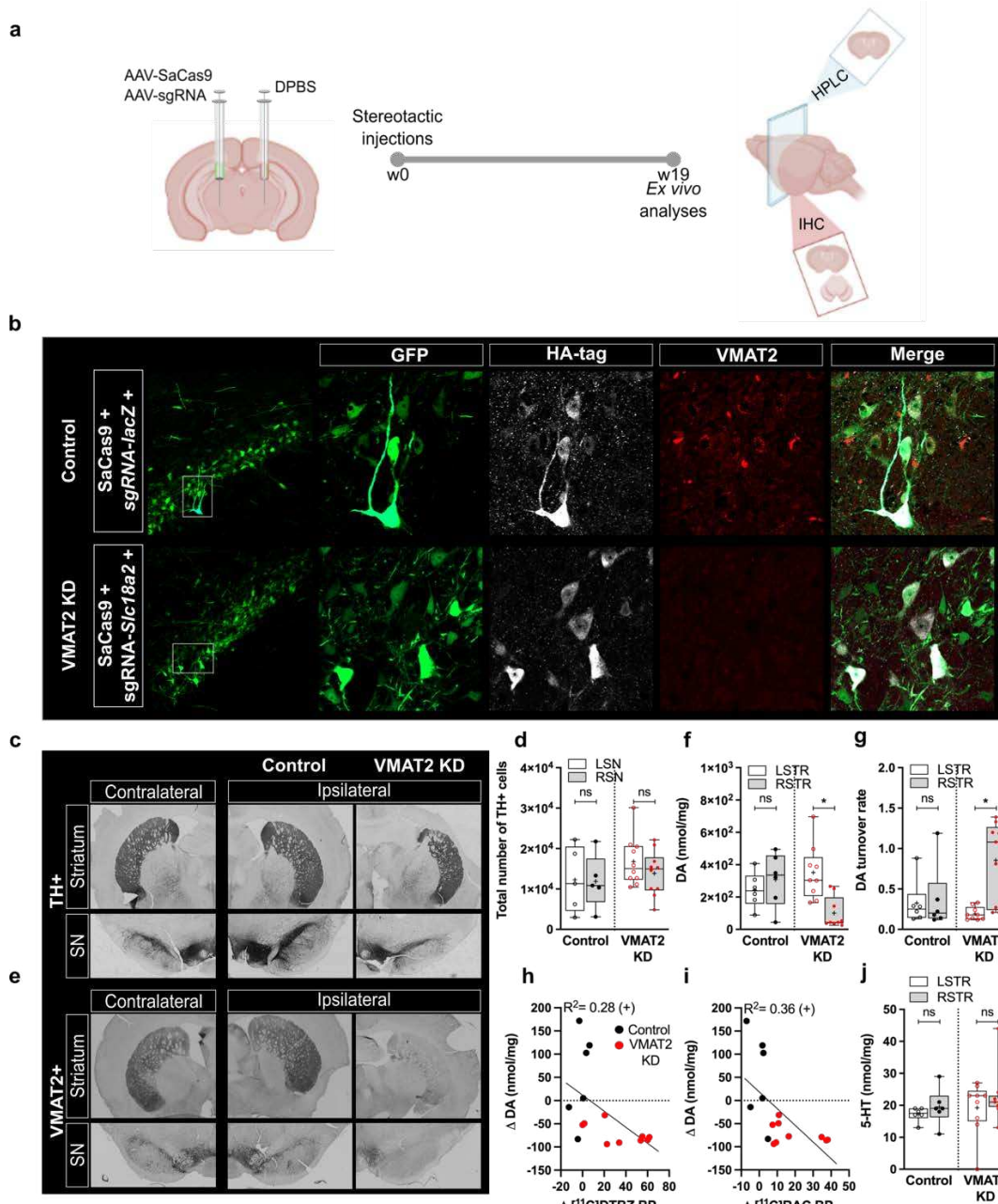
1124



1125
1126 **Fig. 3 CRISPR/SaCas9-induced VMAT2 knockdown impairs motor function.** (a) Schematic illustration
1127 of the behavioral tests. (b) In the open field test, the distance travelled (m) by VMAT2 KD rats was reduced.
1128 (c) Cylinder test. VMAT2 KD rats showed a reduction in the contralateral paw touches, compared with
1129 controls. Rats performance in the cylinder test strongly correlated with VMAT2 expression changes
1130 ($\Delta [^{11}\text{C}]DTBZ$ binding) and corresponding changes in dopamine availability ($\Delta [^{11}\text{C}]RAC$ binding) (d,e). (f) In
1131 the beam walk test, VMAT2 KD rats displayed a higher number of footslips to the left contralateral side
1132 compared with control rats. (g) Body weight assessment 14 weeks after CRISPR/SaCas9 gene-editing
1133 showed reduced body weight gain in VMAT2 KD compared with control rats. (h,i) Body weight gain
1134 correlated with VMAT2 expression changes ($\Delta [^{11}\text{C}]DTBZ$ binding) and corresponding changes in
1135 dopamine availability ($\Delta [^{11}\text{C}]RAC$ binding). (j) Spontaneous rotation in a novel spherical environment
1136 showed increased CW rotations in VMAT2 KD rats compared with control rats. (k) Apomorphine-evoked
1137 rotational behavior. VMAT2 KD rats displayed a higher number of CCW rotations compared with control
1138 rats in the rotameter test. (l,m) Apomorphine-evoked rotations exhibited a strong correlation with VMAT2

1139 expression changes (Δ [^{11}C]DTBZ binding) and changes in dopamine availability (Δ [^{11}C]RAC binding).
1140 Data are shown as boxplot with the median value (central mark), the mean value (plus sign), interquartile
1141 range (boxes edges), and the extreme points of the distribution (whiskers). $^+P<0.05$, $^*P<0.01$, $^{**}P<0.001$.
1142 Control rats n= 8; VMAT2 KD rats n= 12. CCW, counter-clockwise; APO, apomorphine; KD, knockdown;
1143 [^{11}C]RAC, [^{11}C]raclopride. Illustrations in the figure were created with BioRender.com.

1144

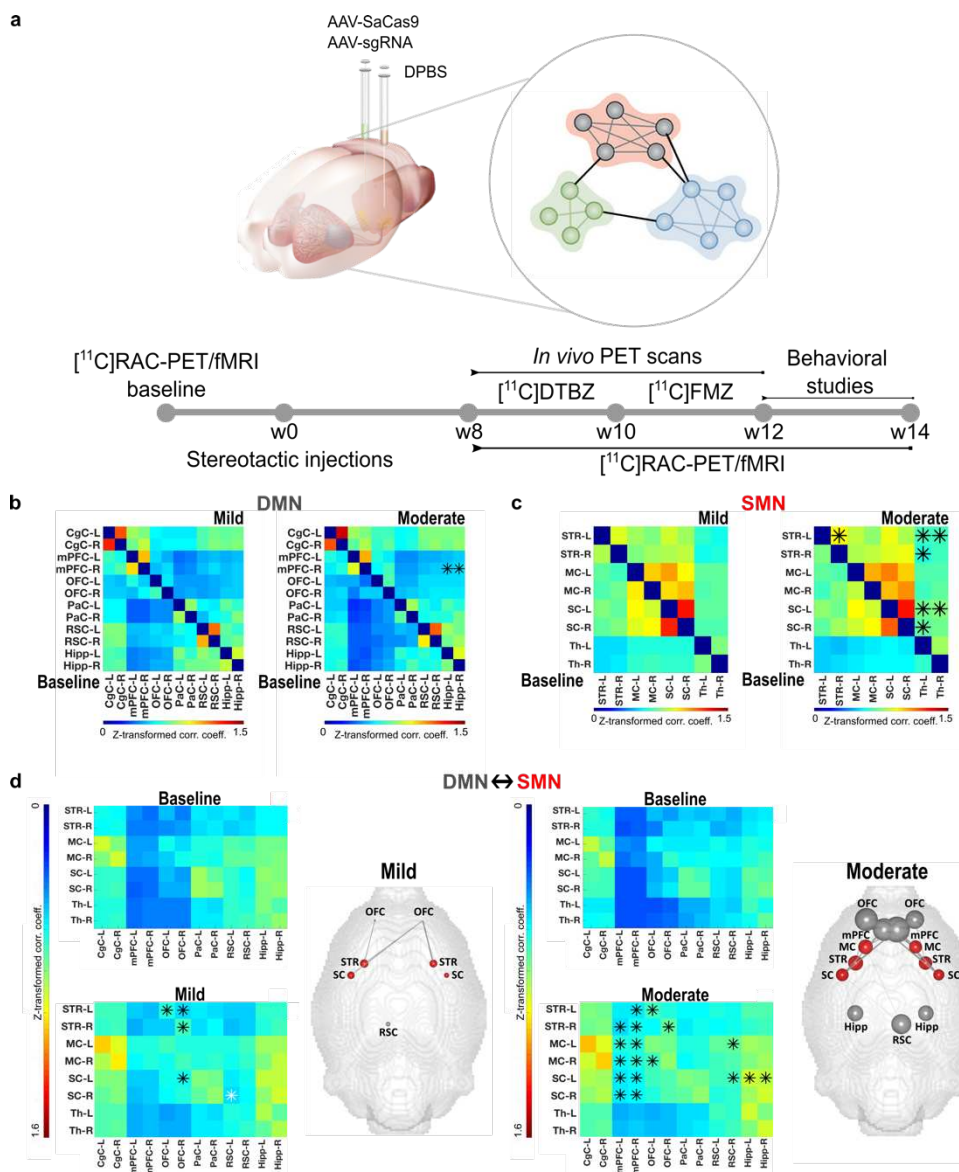


1145

1146 **Fig. 4 Ex vivo validation of the CRISPR/SaCas9-induced VMAT2 knockdown.** (a) Schematic illustration
1147 of the ex vivo analyses. (b) Immunofluorescence of nigral sections of control and VMAT2 KD rats
1148 confirmed the concomitant expression of SaCas9 and sgRNA. Staining for GFP (AAV-sgRNAs, green), HA-
1149 tag (AAV-SaCas9, white), and VMAT2 expression (red) for two exemplary rats is shown. VMAT2
1150 expression was largely reduced in the SNC of VMAT2 KD rats. (c,d) TH expression in the ipsilateral and
1151 contralateral striatum and SNC of VMAT2 KD (n= 10) and control (n= 5) rats evidenced no cell loss. (e)
1152 VMAT2 immunohistochemistry in the SNC and striatum confirmed large protein reduction in the ipsilateral
1153 hemisphere of VMAT2 KD rats. (f) Striatal dopamine, normalized to total protein concentration, was
1154 reduced in the ipsilateral striatum of VMAT2 KD (n= 9), but not control (n= 6) rats. This reduction was
1155 paralleled by increased metabolic outcome (g). (h,i) Dopamine changes correlated with the VMAT2 KD
1156 extent and postsynaptic changes, deducted from [¹¹C]DTBZ and [¹¹C]RAC, respectively. (j) 5-HT content
1157 was unaltered in the striata of control (n= 6) and VMAT2 KD (n= 9) rats. Data are shown as boxplot with the

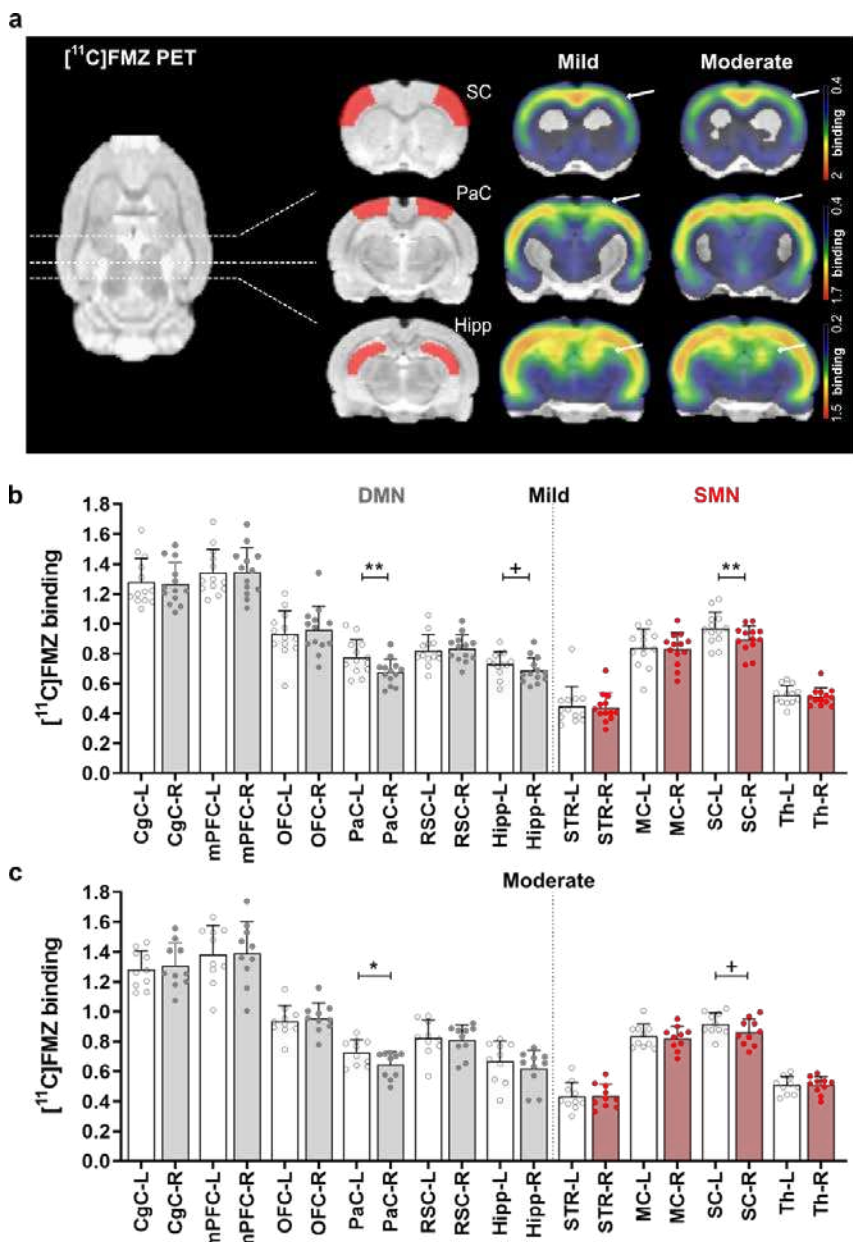
1158 median value (central mark), the mean value (plus sign), interquartile range (boxes edges), and the
1159 extreme points of the distribution (whiskers). $^+P < 0.05$, $^*P < 0.01$. GFP, green fluorescent protein; HA-tag,
1160 hemagglutinin tag; KD, knockdown; TH, tyrosine hydroxylase; SN, substantia nigra; STR, striatum;
1161 [^{11}C]RAC, [^{11}C]raclopride; DA, dopamine; 5-HT, serotonin. Metabolites' and neurotransmitters' striatal
1162 content is reported in Table 3. Illustrations in the figure were created with BioRender.com.

1163



1164

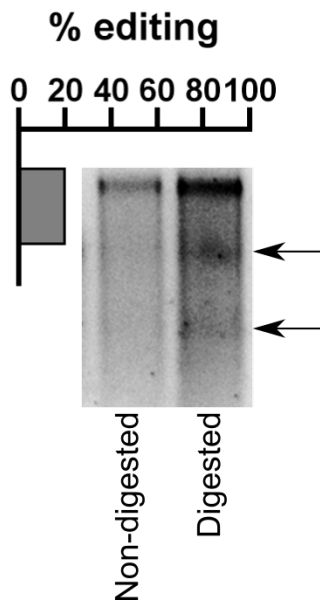
1165 **Fig. 5 Increased resting-state functional connectivity after CRISPR/SaCas9-induced VMAT2**
1166 **knockdown.** (a) Schematic illustration of the experimental design. Group level correlation matrices of the
1167 DMN (b) and SMN (c) at baseline and after CRISPR/SaCas9-targeting for rats with a *mild* (left panel) and
1168 *moderate* (right panel) VMAT2 KD. In the *moderate* KD group rs-FC was increased between the right
1169 mPFC and right and left Hipp in the DMN (b) and between the contralateral SC and right and left Th, as
1170 well as between the left STR and right and left Th, in the SMN (c). (d) Internetwork rs-FC changes in the
1171 *mild* KD group indicated increased rs-FC between anterior regions of the DMN and the SMN (between the
1172 left OFC and STR, and between the right OFC and the left SC, and the right and left STR). Conversely, rs-
1173 FC was decreased between regions of the posterior DMN and the SMN (between the left RSC and right
1174 SC). In the *moderate* KD group, DMN-SMN rs-FC was increased. Brain graphs, right to the matrices,
1175 illustrate the nodes and edges (raw values) that demonstrated rs-FC changes to baseline (%). * $P < 0.01$.
1176 *Mild*: Δ [¹¹C]DTBZ binding < 20%, n=13; *Moderate*: Δ [¹¹C]DTBZ binding \geq 20%, n=10. KD, knockdown;
1177 DMN, default-mode network; SMN, sensorimotor network. mPFC, medial prefrontal cortex; Hipp,
1178 hippocampus; SC, somatosensory cortex; Th, thalamus; STR, striatum; OFC, orbitofrontal cortex; RSC,
1179 retrosplenial cortex. Abbreviations of brain regions considered for the analysis of the fMRI data, including
1180 their respective volumes, are reported in Table 2.



1181
1182
1183
1184
1185
1186
1187
1188
1189
1190
1191
1192

Fig. 6 CRISPR/SaCas9-induced VMAT2 knockdown alters GABA signaling. (a) [¹¹C]FMZ mean binding potential maps of *mild* and *moderate* VMAT2 KD rats co-registered to a rat brain atlas. Arrows and ROIs in coronal sections indicate brain regions of the DMN and SMN with altered [¹¹C]FMZ binding. [¹¹C]FMZ binding potentials from VOI-based analysis in DMN and SMN regions of rats with *mild* (b) and *moderate* (c) VMAT2 KD. [¹¹C]FMZ binding was decreased in the right PaC, SC, and Hipp of *mild* KD rats (b) and right PaC and SC of *moderate* KD rats (c). *P< 0.05, **P< 0.01, **P< 0.001, Bonferroni-Sidak corrected. Data are shown as mean \pm SD. *Mild*: Δ [¹¹C]DTBZ binding < 20%, n= 13; *Moderate*: Δ [¹¹C]DTBZ binding \geq 20%, n= 10. KD, knockdown; [¹¹C]FMZ, [¹¹C]flumazenil; DMN, default-mode network; SMN, sensorimotor network. PaC, parietal cortex; Hipp, hippocampus; SC; somatosensory cortex. Abbreviations of brain regions, including their respective volumes, are reported in Table 2.

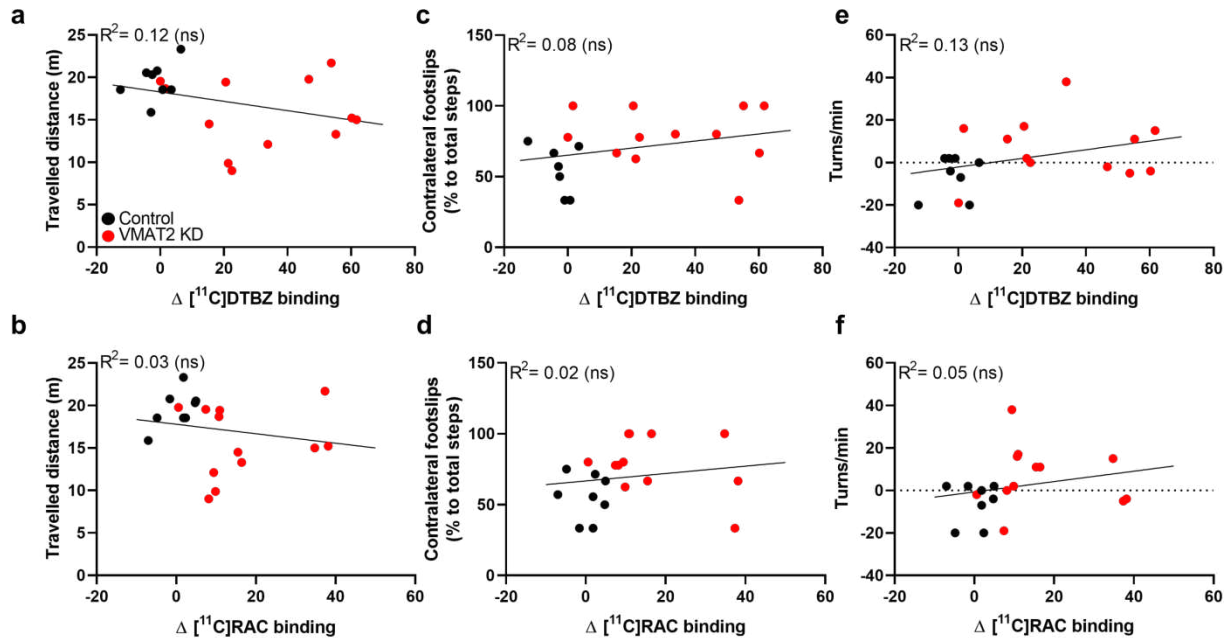
1193 **Supplementary Figures**



1194

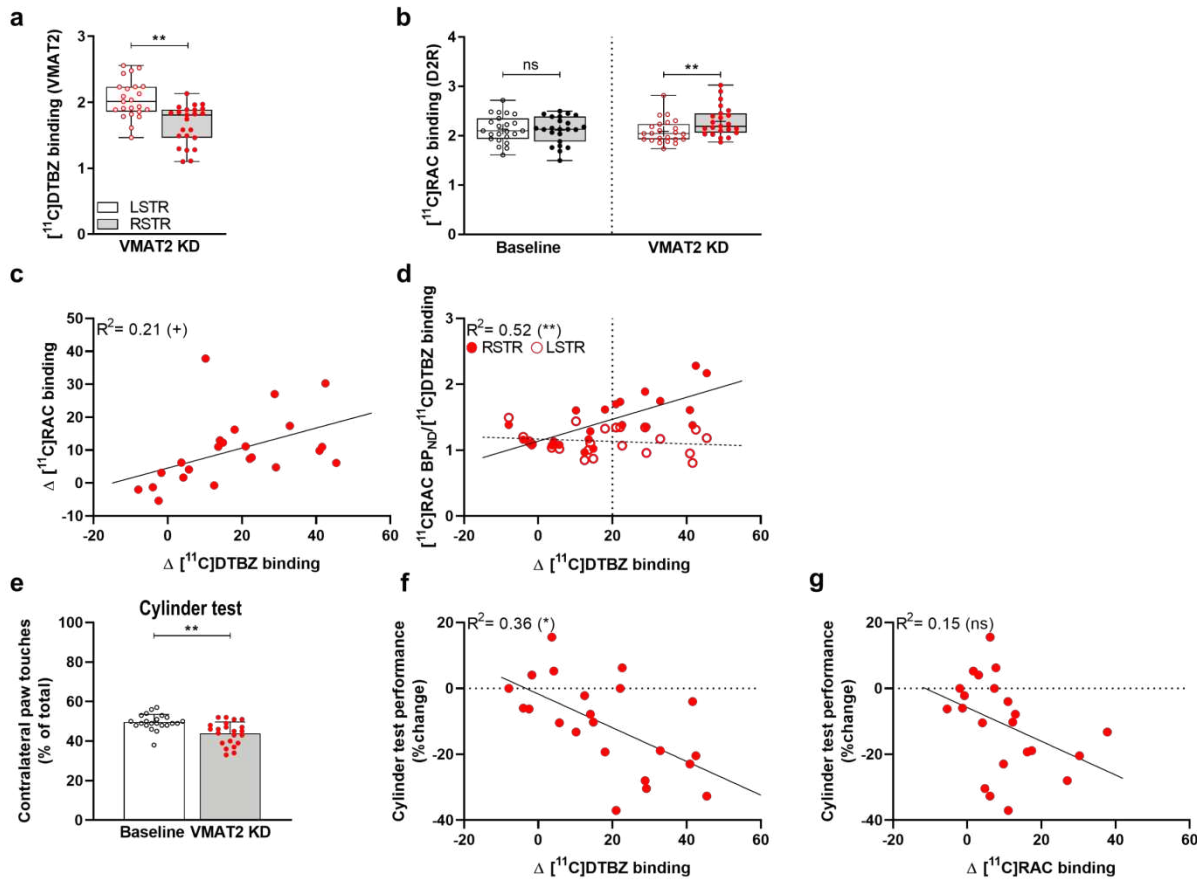
1195 **Supplementary Fig. 1 *In vitro* validation of CRISPR/SaCas9-induced VMAT2 knockdown in rat**
1196 **primary cortical neurons.** One-week post-transduction with conditional vectors for SaCas9 and sgRNA-
1197 *Slc18a2*, neurons were processed for the Surveyor assay. The expected cleavage products (arrows), and
1198 estimated editing of 20%, could be seen for the digested DNA.

1199



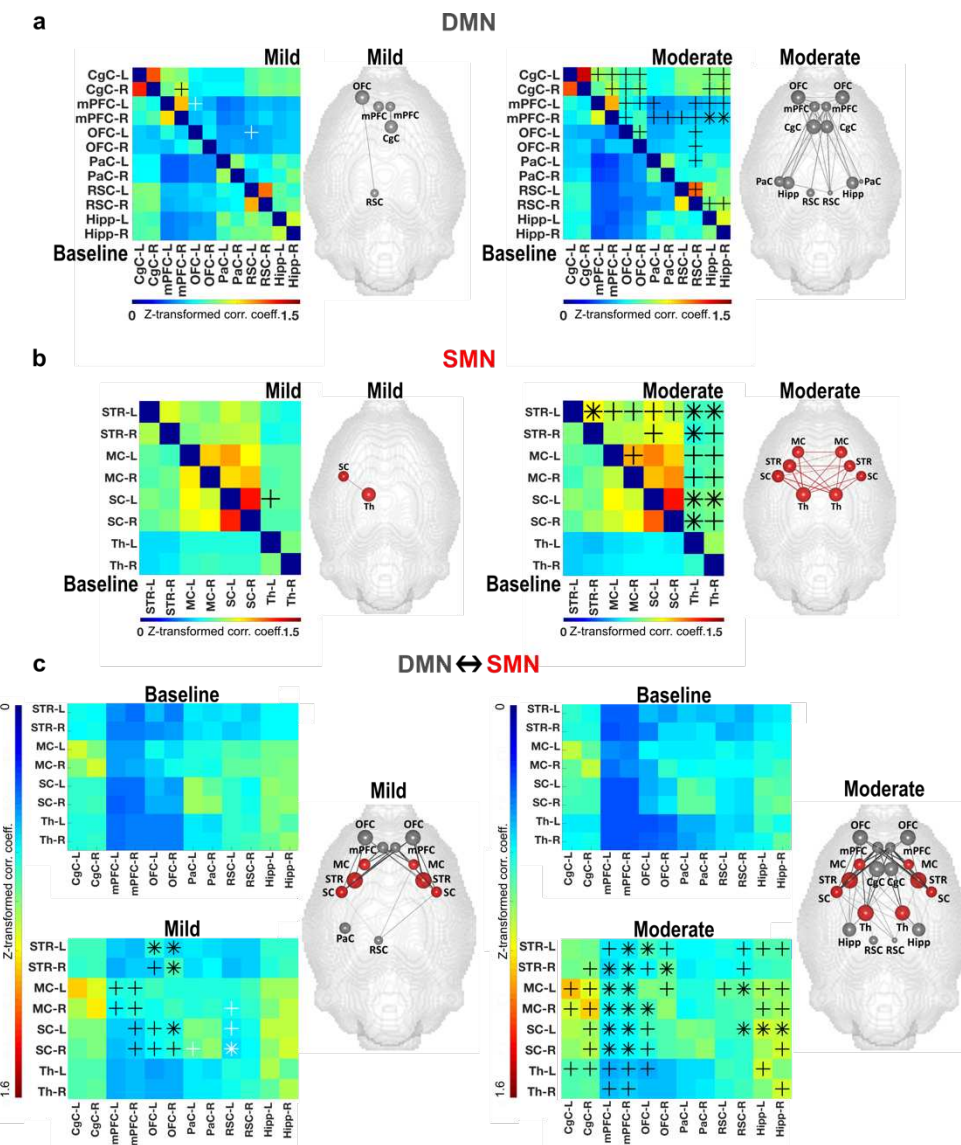
1200
1201
1202
1203
1204
1205
1206
1207
1208
1209

Supplementary Fig. 2 CRISPR/SaCas9-induced VMAT2 knockdown, postsynaptic changes, and motor impairment do not correlate for whole-body movements. No correlation was observed between locomotor activity and (a) VMAT2 expression changes ($\Delta [11\text{C}]DTBZ$ binding), or (b) dopamine availability ($\Delta [11\text{C}]RAC$ binding). The number of contralateral footslips in the beam walk test did not correlate with (c) changes in VMAT2 expression ($\Delta [11\text{C}]DTBZ$ binding) or (d) dopamine availability ($\Delta [11\text{C}]RAC$ binding). Spontaneous rotations did not correlate with (e) changes in VMAT2 expression ($\Delta [11\text{C}]DTBZ$ binding) or (f) dopamine availability ($\Delta [11\text{C}]RAC$ binding). ns $P \geq 0.05$. Control rats $n=8$; VMAT2 KD rats $n=12$. KD, knockdown; $[11\text{C}]RAC$, $[11\text{C}]$ raclopride.



1210
1211
1212
1213
1214
1215
1216
1217
1218
1219
1220
1221
1222
1223

Supplementary Fig. 3 Reproducibility of the CRISPR/SaCas9-induced VMAT2 knockdown. (a) $[^{11}\text{C}]DTBZ$ in VMAT2 KD rats and (b) $[^{11}\text{C}]RAC$ PET at baseline and after CRISPR/SaCas9-induced VMAT2 KD. (c) A strong correlation between $\Delta [^{11}\text{C}]RAC$ and $\Delta [^{11}\text{C}]DTBZ$ binding is shown. (d) At 20% VMAT2 KD ($\Delta [^{11}\text{C}]DTBZ$ binding), D2R binding ($\Delta [^{11}\text{C}]RAC$ binding) prominently increased. This threshold was therefore set to separate the rats into *mild* and *moderate*. Data are shown as boxplot with the median value (central mark), the mean value (plus sign), interquartile range (boxes edges), and the extreme points of the distribution (whiskers). Baseline n= 23, VMAT2 KD n= 23. (e) Cylinder test at baseline (n= 22) and 12 - 14 weeks after CRISPR/SaCas9 gene-editing (n= 22). VMAT2 KD rats showed reduced contralateral paw touches compared to baseline. Rats performance in the cylinder test, % change from baseline, correlated with reduced VMAT2 expression ($\Delta [^{11}\text{C}]DTBZ$ binding) (f), but not with dopamine availability ($\Delta [^{11}\text{C}]RAC$ binding) (g). Data are shown as mean \pm SD. $^+P < 0.05$, $^*P < 0.01$, $^{**}P < 0.001$. KD, knockdown; $[^{11}\text{C}]RAC$, $[^{11}\text{C}]raclopride.$

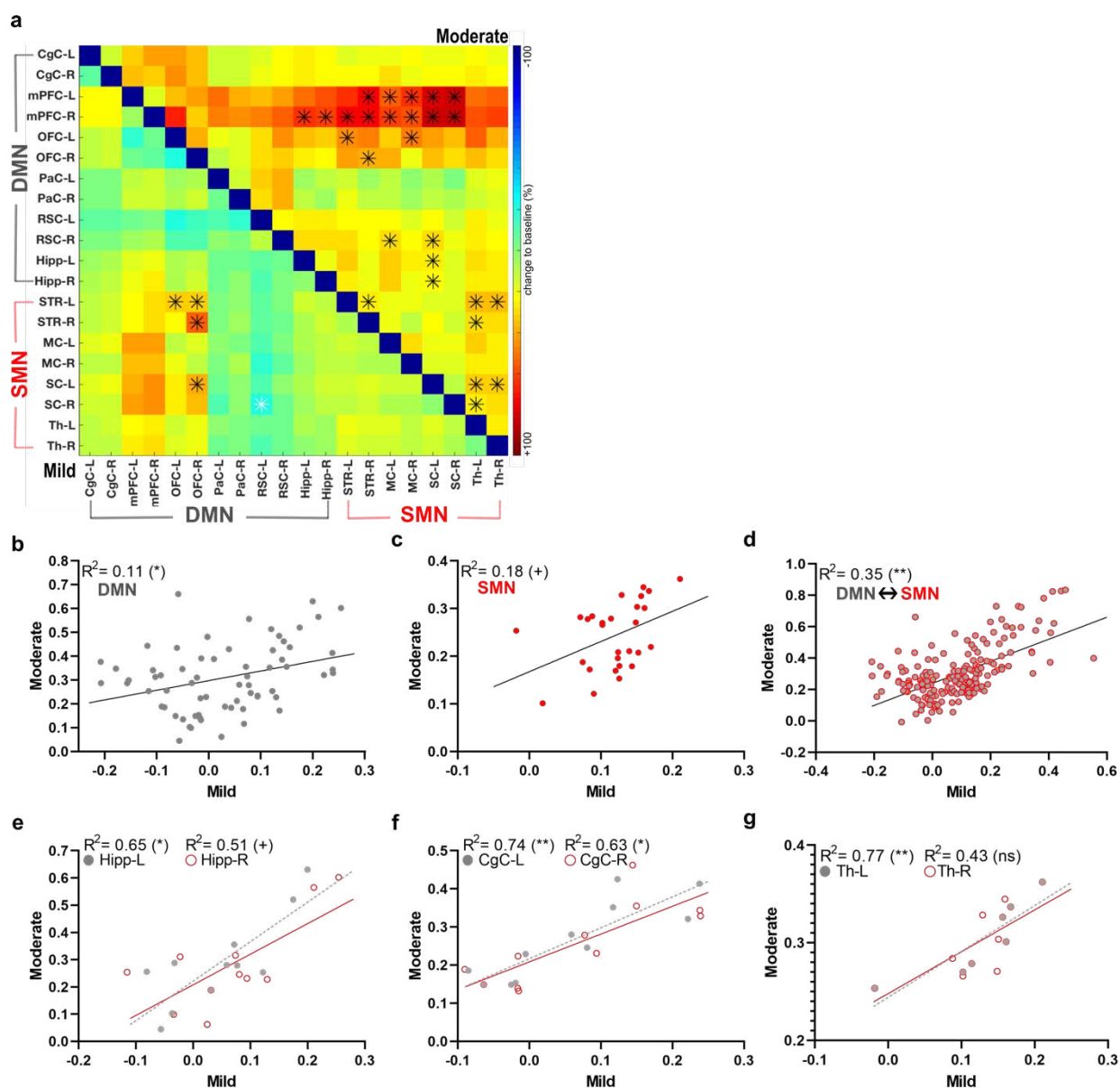


1224

1225 **Supplementary Fig. 4 Increased resting-state functional connectivity after CRISPR/SaCas9-induced**
1226 **VMAT2 knockdown.** Group level correlation matrices of the DMN (a) and SMN (b) at baseline and after
1227 VMAT2 KD for *mild* (left panel) and *moderate* (right panel) rats. Brain graphs, right to the matrices, illustrate
1228 the nodes and edges (raw values) that demonstrated rs-FC changes to baseline (%) in DMN (a) and SMN
1229 (b). (a) In rats with *mild* VMAT2 KD, we observed divergent rs-FC changes to baseline in regions of the
1230 anterior DMN (left mPFC and OFC, right mPFC and CgC). In rats with *moderate* VMAT2 KD, we observed
1231 rs-FC increase in most regions of the anterior DMN, extending to the posterior DMN (RSC bilaterally, right
1232 RSC, and Hipp bilaterally). (b) In rats with *mild* VMAT2 KD, we observed rs-FC increase between the
1233 contralateral SC and Th, which intensified in *moderate* VMAT2 KD rats and extended to most of the regions
1234 of the SMN. (c) Group level correlation matrices of the DMN-SMN rs-FC changes at baseline and after
1235 VMAT2 KD for *mild* (left panel) and *moderate* (right panel) rats. Brain graphs, right to the matrices, illustrate
1236 the nodes and edges (raw values) that demonstrated internetwork rs-FC changes to baseline (%).
1237 Internetwork FC changes in rats with *mild* VMAT2 KD indicated increased rs-FC between anterior regions
1238 of the DMN and the SMN (between OFC and STR, SC bilaterally, between right mPFC and MC, SC
1239 bilaterally), and decreased rs-FC between posterior regions of the DMN and the SMN (between left RSC
1240 and right MC, and SC bilaterally). Increased DMN-SMN rs-FC was found in rats with *moderate* VMAT2 KD.

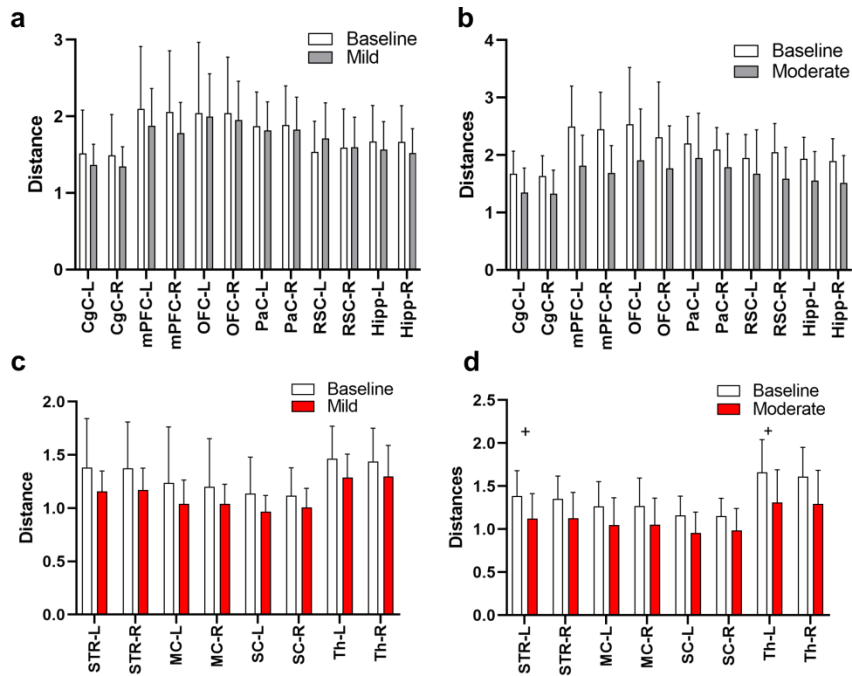
1241 Internetwork rs-FC alterations extended between CgC/Hipp, and SC, MC, Th. ${}^+P<0.05$, ${}^*P<0.01$. *Mild*:
1242 $\Delta[{}^{11}\text{C}]DTBZ$ binding $<20\%$, $n=13$; *Moderate*: $\Delta[{}^{11}\text{C}]DTBZ$ binding $\geq 20\%$, $n=10$. KD, knockdown; DMN,
1243 default-mode network; SMN, sensorimotor network. mPFC, medial prefrontal cortex; OFC, orbitofrontal
1244 cortex; CgC, cingulate cortex; RSC, retrosplenial cortex; Hipp, hippocampus; SC, somatosensory cortex;
1245 Th, thalamus; STR, striatum; MC, motor cortex. Abbreviations of brain regions considered for the analysis
1246 of the fMRI data, including their respective volumes, are reported in Table 2.

1247



1248
1249
1250
1251
1252
1253
1254
1255
1256
1257
1258
1259
1260
1261
1262

Supplementary Fig. 5 Node correlation analyses evidence pattern similarity and a linear relationship between the magnitude of the resting-state functional connectivity changes in *mild* and *moderate* rats. (a) Group level correlation matrices of the intraregional and internetwork rs-FC changes to baseline (%) for *mild* and *moderate* VMAT2 KD rats. (b-d) Group level intraregional and internetwork rs-FC changes correlated linearly between the two groups. Node correlation analysis between *mild* and *moderate* VMAT2 KD rats indicated a linear increase in the magnitude of the rs-FC changes to baseline in the right and left Hipp (e), and CgC (f). (g) Rs-FC changes (%) in the SMN correlated linearly between *mild* and *moderate* VMAT2 KD rats in the left, but not in the right Th. Our data suggest a similarity in the pattern of the intraregional and internetwork rs-FC changes between rats with *mild* and *moderate* VMAT2 KD and a linear relationship between the magnitude of the rs-FC changes. ${}^+P<0.05$, ${}^*P<0.01$, ${}^{**}P<0.001$. *Mild*: $\Delta[{}^{11}\text{C}]DTBZ$ binding $<20\%$, $n=13$; *Moderate*: $\Delta[{}^{11}\text{C}]DTBZ$ binding $\geq20\%$, $n=10$. KD, knockdown; DMN, default-mode network; SMN, sensorimotor network. Hipp, hippocampus; CgC, cingulate cortex. Th, thalamus. Abbreviations of brain regions considered for the analysis of the fMRI data, including their respective volumes, are reported in Table 2.



1263

1264 **Supplementary Fig. 6 Graph theoretical analyses reveal lateralized recruitment of SMN regions**
1265 **following the CRISPR/SaCas9-induced VMAT2 moderate knockdown.** Quantitative graph theoretical
1266 analyses of the global mean connection distance indicated no changes for *mild* (a) and *moderate* (b)
1267 VMAT2 KD rats in the DMN. (c) Rats with *mild* VMAT2 KD displayed no changes in the SMN. (d) Instead,
1268 rats with *moderate* VMAT2 KD presented shorter functional paths to the nodes in the contralateral Th and
1269 STR. Data are shown as mean \pm SD. $^+$ $P < 0.05$, Bonferroni-Sidak-corrected. *Mild*: Δ [11 C]DTBZ binding
1270 $< 20\%$, $n = 13$; *Moderate*: Δ [11 C]DTBZ binding $\geq 20\%$, $n = 10$. KD, knockdown; DMN: default-mode network,
1271 SMN: sensorimotor network; Th: Thalamus; STR: striatum. Abbreviations of brain regions considered for
1272 the analysis of the fMRI data, including their respective volumes, are reported in Table 2.

1273

1274 **Tables**

1275 **Table 1: sgRNAs sequences.**

1276

SgRNAs	DNA Target Sequences 5'- 3'	PAM (NNGRRT) 5'- 3'
<i>Slc18a2</i>	CGATGAACAGGATCAGTTGC	GCGAGT
<i>lacZ</i>	CCTTCCCAACAGTTGCGCAGC	CTGAAT

1279

1280

1281

1282

1283

1284

1285

1286

1287

1288

1289 **Table 2: Brain regions included in the Paxinos rat brain atlas, including their respective volumes**
1290 **and abbreviations.**

Brain region (ROI)	Hemisphere	ROI volume [mm ³]	Abbreviation
Striatum	left	43.552	STR
	right		
Cingulate Cortex	left	14.480	CgC
	right		
Medial Prefrontal Cortex	left	6.304	mPFC
	right		
Motor Cortex	left	32.608	MC
	right		
Orbitofrontal Cortex	left	18.936	OFC
	right		
Parietal Cortex	left	7.632	PaC
	right		
Retrosplenial Cortex	left	18.920	RSC
	right		
Somatosensory Cortex	left	71.600	SC
	right		
Hippocampus	left	25.064	Hipp
	right		
Thalamus	left	30.712	Th
	right		

1291

1292 **Table 3: Dopamine, 3,4-Dihydroxyphenylacetic acid (DOPAC), homovanillic acid (HVA), and**
1293 **serotonin (5-HT) striatal content (nmol/mg) determined by HPLC.**

Neurotransmitter or Metabolite	nmol/mg (mean \pm SD)	
DA	Control	VMAT2 KD
STR-L	244 \pm 109	351 \pm 168
STR-R	308 \pm 166	100 \pm 97
DOPAC	Control	VMAT2 KD
STR-L	34 \pm 7	34 \pm 11
STR-R	38 \pm 4	27 \pm 5
HVA	Control	VMAT2 KD
STR-L	24 \pm 5	25 \pm 5
STR-R	26 \pm 6	19 \pm 4
5-HT	Control	VMAT2 KD
STR-L	17 \pm 2	19 \pm 8
STR-R	19 \pm 6	23 \pm 9

1294

1295

1296 **Supplementary Tables**

1297 **Supplementary Table 1: *P* values of the functional connectivity changes in regions of the DMN for**
1298 **rats with *mild* VMAT2 knockdown. Data were analyzed using paired t-tests.**

<i>Mild</i>	Hipp-R	Hipp-L	RSC-R	RSC-L	PaC-R	PaC-L	OFC-R	OFC-L	mPFC-R	mPFC-L	CgC-R
CgC-L	0.40	0.56	0.95	0.33	0.76	0.84	0.22	0.27	0.07	0.07	0.61
CgC-R	0.30	0.41	0.83	0.29	0.84	0.86	0.17	0.23	0.03	0.08	
mPFC-L	0.21	0.34	0.77	0.73	0.36	0.55	0.46	0.02	0.53		
mPFC-R	0.12	0.23	0.54	0.99	0.24	0.46	0.24	0.61			
OFC-L	0.49	0.55	0.20	0.05	0.51	0.67	0.18				
OFC-R	0.31	0.20	0.26	0.13	0.23	0.45					
PaC-L	0.61	0.39	0.84	0.08	0.31						
PaC-R	0.74	0.59	0.83	0.11							
RSC-L	0.18	0.22	0.31								
RSC-R	0.75	0.65									
Hipp-L	0.67										

1299
1300 **Supplementary Table 2: *P* values of the functional connectivity changes in regions of the DMN for**
1301 **rats with *moderate* VMAT2 knockdown. Data were analyzed using paired t-tests.**

<i>Moderate</i>	Hipp-R	Hipp-L	RSC-R	RSC-L	PaC-R	PaC-L	OFC-R	OFC-L	mPFC-R	mPFC-L	CgC-R
CgC-L	0.05	0.02	0.07	0.11	0.24	0.22	0.05	0.03	0.03	0.04	0.07
CgC-R	0.03	0.02	0.08	0.14	0.21	0.25	0.04	0.01	0.03	0.05	
mPFC-L	0.01	0.03	0.03	0.09	0.05	0.04	0.04	0.04	0.06		
mPFC-R	0.005	0.007	0.01	0.03	0.03	0.03	0.06	0.01			
OFC-L	0.08	0.10	0.04	0.13	0.24	0.21	0.05				
OFC-R	0.16	0.11	0.03	0.07	0.29	0.47					
PaC-L	0.35	0.60	0.03	0.10	0.13						
PaC-R	0.42	0.32	0.06	0.22							
RSC-L	0.10	0.07	0.02								
RSC-R	0.03	0.04									
Hipp-L	0.15										

1318
1319
1320
1321
1322
1323
1324
1325
1326
1327

1328 **Supplementary Table 3: *P* values of the functional connectivity changes in regions of the SMN for**
 1329 **rats with *mild* VMAT2 knockdown. Data were analyzed using paired t-tests.**
 1330

<i>Mild</i>	Th-R	Th-L	SC-R	SC-L	MC-R	MC-L	STR-R
STR-L	0.13	0.06	0.21	0.14	0.23	0.21	0.39
STR-R	0.13	0.09	0.19	0.13	0.39	0.29	
MC-L	0.24	0.16	0.47	0.16	0.46		
MC-R	0.29	0.23	0.38	0.21			
SC-L	0.14	0.04	0.76				
SC-R	0.30	0.12					
Th-L	0.79						
Th-R							

1331
 1332 **Supplementary Table 4: *P* values of the functional connectivity changes in regions of the SMN for**
 1333 **rats with *moderate* VMAT2 knockdown. Data were analyzed using paired t-tests.**
 1334

<i>Moderate</i>	Th-R	Th-L	SC-R	SC-L	MC-R	MC-L	STR-R
STR-L	0.01	0.004	0.02	0.05	0.03	0.04	0.007
STR-R	0.02	0.008	0.06	0.04	0.16	0.07	
MC-L	0.04	0.01	0.10	0.08	0.04		
MC-R	0.02	0.02	0.07				
SC-L	0.003	0.001	0.11				
SC-R	0.02	0.008					
Th-L	0.07						
Th-R							

1335
 1336 **Supplementary Table 5: *P* values of the functional connectivity internetwork changes in regions of**
 1337 **the DMN and SMN for rats with *mild* VMAT2 knockdown. Data were analyzed using paired t-tests.**
 1338

<i>Mild</i>	Hipp-R	Hipp-L	RSC-R	RSC-L	PaC-R	PaC-L	OFC-R	OFC-L	mPFC-R	mPFC-L	CgC-R	CgC-L
STR-L	0.23	0.18	0.82	0.26	0.94	0.93	0.006	0.005	0.10	0.15	0.27	0.29
STR-R	0.16	0.44	0.65	0.32	0.65	0.98	0.0004	0.03	0.06	0.19	0.24	0.31
MC-L	0.34	0.39	0.92	0.29	0.93	0.94	0.11	0.40	0.02	0.04	0.10	0.07
MC-R	0.26	0.60	0.18	0.04	0.49	0.88	0.37	0.16	0.02	0.05	0.18	0.35
SC-L	0.12	0.26	0.78	0.05	0.87	0.46	0.002	0.02	0.03	0.05	0.13	0.17
SC-R	0.13	0.57	0.19	0.006	0.89	0.04	0.01	0.04	0.02	0.06	0.18	0.28
Th-L	0.35	0.27	0.55	0.39	1.00	0.89	0.09	0.21	0.11	0.17	0.14	0.17
Th-R	0.38	0.98	0.66	0.26	0.94	0.70	0.09	0.15	0.09	0.11	0.28	0.33

1339
 1340

1341 **Supplementary Table 6: *P* values of the functional connectivity internetwork changes in regions of**
 1342 **the DMN and SMN for rats with *moderate* VMAT2 knockdown. Data were analyzed using paired t-**
 1343 **tests.**

1344

<i>Moderate</i>	Hipp-R	Hipp-L	RSC-R	RSC-L	PaC-R	PaC-L	OFC-R	OFC-L	mPFC-R	mPFC-L	CgC-R	CgC-L
STR-L	0.02	0.02	0.02	0.11	0.16	0.30	0.03	0.003	0.006	0.01	0.07	0.09
STR-R	0.08	0.08	0.04	0.14	0.30	0.63	0.008	0.01	0.002	0.003	0.04	0.07
MC-L	0.03	0.03	0.003	0.03	0.45	0.46	0.04	0.07	0.003	0.003	0.02	0.02
MC-R	0.03	0.05	0.05	0.18	0.52	0.97	0.19	0.008	0.01	0.007	0.03	0.03
SC-L	0.004	0.008	0.008	0.08	0.11	0.44	0.05	0.02	0.003	0.004	0.04	0.06
SC-R	0.02	0.08	0.06	0.35	0.27	0.94	0.07	0.04	0.001	0.003	0.04	0.07
Th-L	0.06	0.02	0.09	0.10	0.17	0.15	0.06	0.03	0.02	0.03	0.03	0.04
Th-R	0.03	0.10	0.09	0.23	0.15	0.13	0.14	0.08	0.02	0.04	0.07	0.15

1345

1346

1347

1348

1349

Supplementary Table 7: Bonferroni-Sidak corrected *P* values for graph theoretical measures of the global mean connection distance in *mild* and *moderate* VMAT2 knockdown rats. Data were analyzed using paired t-tests.

Region	<i>Mild</i>	<i>Moderate</i>
CgC-L	0.39	0.48
CgC-R	0.37	0.45
mPFC-L	0.41	0.24
mPFC-R	0.28	0.10
OFC-L	0.87	0.81
OFC-R	0.67	0.89
PaC-L	0.68	0.96
PaC-R	0.66	0.83
RSC-L	0.18	0.96
RSC-R	0.97	0.38
Hipp-L	0.50	0.42
Hipp-R	0.34	0.35
STR-L	0.15	0.01
STR-R	0.18	0.09
MC-L	0.27	0.64
MC-R	0.29	0.48
SC-L	0.16	0.08
SC-R	0.29	0.35
Th-L	0.12	0.03
Th-R	0.28	0.09

1350

1351

1352 **Supplementary Table 8: Primers used to amplify the *Slc18a2* and the *lacZ* loci in the Surveyor assay**
1353 **and DNA expected fragments sizes.**

SgRNAs	Forward Primer 5'- 3'	Reverse Primer 5'- 3'	Fragment size (bp)
<i>Slc18a2</i>	CTTGGGGATCCTCTAAGGCAG	TACAGCGCGGTTCTCAACT	313_280
<i>lacZ</i>	GTCGTGACTGGGAAAACCCT	TTGTTCCCACGGAGAACCG	200_80

1354
1355 **Supplementary Table 9: [¹¹C]DTBZ, [¹¹C]methylphenidate, [¹¹C]raclopride and [¹⁸F]GE-180 injected**
1356 **and molar activities.**

1357 1358 Radioligand	1359 Injected Activity (Mean ± SD) 1360 MBq	1361 Molar Activity (Mean ± SD) 1362 GBq/μmol
[¹¹ C]DTBZ	25 ± 1	93 ± 35
[¹¹ C]MP	25 ± 1	57 ± 14
[¹¹ C]RAC	25 ± 1	88 ± 41
[¹⁸ F]GE-180	24 ± 3	576 ± 283

1366
1367 **Supplementary Table 10: [¹¹C]raclopride, [¹¹C]DTBZ, [¹¹C]flumazenil injected and molar activities.**

1368 Radioligand	1369 Injected Activity (Mean ± SD) 1370 MBq	1371 Molar Activity (Mean ± SD) 1372 GBq/μmol
[¹¹ C]RAC t0	27 ± 4	108 ± 49
[¹¹ C]RAC t8	28 ± 1	115 ± 41
[¹¹ C]DTBZ	27 ± 1	180 ± 48
[¹¹ C]FMZ	27 ± 1	109 ± 40